A MD STUDY OF Sn AND ITS CRYSTAL - MELT INTERFACE PROPERTIES

A MD STUDY OF Sn AND ITS CRYSTAL - MELT INTERFACE PROPERTIES

By

SHAON YASMIN, B. Sc (Engineering)

A Thesis

Submitted to the School of Graduate Studies

in Partial Fulfillment of the Requirements

for the Degree

Master of Applied Science

McMaster University

MASTER OF APPLIED SCIENCE (2010) McMaster University

(Materials Science and Engineering) Hamilton, Ontario

TITLE: A MD study of Sn and its crystal – melt interface properties

AUTHOR: Shaon Yasmin, B. Eng (Bangladesh University of Engineering and Technology, Bangladesh)

SUPERVISOR: Dr. Jeffrey J. Hoyt

NUMBER OF PAGES: xiii, 87

Abstract

The unique combination of material properties has led to the extensive use of Sn in a wide range of industrial applications, making it one of the most important commercial materials. In this research work, an atomic scale computational model has been developed for Sn using Molecular Dynamics (MD). The MD simulation technique has proven to be quite effective in establishing quantitative models for different materials. But accurately modeling Sn using classical interatomic potentials in MD is quite difficult due to its complex crystal structure and phase stability. The Modified Embedded Atom Method (MEAM) has been used in this study as it includes angular forces present in materials with directional bonding, which can model both the metallic and covalent phase of Sn. Using this method, a previously published pure Sn potential has been modified to improve upon the melting properties. Some predictions are presented for thermodynamic quantities, phase stability, structural properties and elastic constants. Good agreement has been found with experiments for the melting point, the phase transition temperature and the latent heats; however the predicted elastic constants are somewhat greater than those found in the literature. The crystal – melt interface and its properties are also investigated with the new potential. The (001)[100] orientation of the interface is found to be atomically rough. Capillary Fluctuation Method (CFM) is used to compute the crystal – melt interface stiffness in this orientation and the interface kinetics is investigated with CFM and Free Solidification (FS) technique. The (100)[010]

and $(110)[1\bar{1}0]$ oriented interface is found to be flat or atomically smooth. Wulff plot is constructed to determine the equilibrium shape of a single Sn crystal and an approximate measurement of the interfacial energy for the flat interfaces is presented.

Acknowledgement

At first, I would like to offer my sincere gratitude to my supervisor, Dr. Jeffrey J. Hoyt for his continuous guidance, invaluable assistance and support throughout my stay at McMaster. I am indebted to him for his constructive suggestions and valuable instructions to overcome the critical problems that arose during this research work. I attribute the level of this study to his encouragement, patience and relentless efforts.

This research work was carried out using the high performance computing resources of Shared Hierarchical Academic Research Computing Network (SHARCNET). I would like to acknowledge SHARCNET Help Desk for providing instant feedback on different technical issues. My appreciation also goes to Mr. Ed McCaffery, laboratory manager, MSE department for his assistance to solve all kinds of computer related problems.

It was a pleasure to work with the research group of Dr. Hoyt. This research work was greatly benefitted from the weekly group meetings and the productive discussions among the members. I would also like to thank my fellow colleagues for their incessant support and great company.

I wish to take this opportunity to thank my family for their love and encouragement. My parents, who have inspired me and guided me at each and every step of my life, showered me with their eternal love and supported me in all my pursuits. And last, but not the least, my heartfelt thanks to my husband, Abdullah, for his love, patience and encouragement to complete my MASc.

Table of Contents

List of Figures

Chapter – 1

Chapter – 2

Chapter – 4

List of Tables

CHAPTER 1

Introduction

1.1 Importance of Sn and Its Alloys

Over the last few decades, industrial applications of tin (Sn) and its alloys have increased rapidly making it one of the most important commercial materials. It possesses a unique combination of properties, which has led to its use in a wide range of applications. Sn is rarely used in its pure form because of its softness; it is almost always used in combination with other metals, either as an alloying element or as a coating. According to a report by the International Tin Research Institute (ITRI)[1], world refined Sn usage reached an all-time record level of 363,100 tons in 2007. As can be seen from figure – 1.1, the two most significant uses of Sn are in solders and tinplate. Roughly two thirds of the Sn consumed by the solder market is used in the electronic industry as a major component of the next generation lead free solder [2]. The development of lead free solder alternatives was initially driven by impending U.S. legislation and Environmental Protection Agency regulations restricting lead usage in the electronics industry due to its toxicity. After July 1, 2006, the European RoHS has prohibited the sale of electrical and electronic equipment containing Pb and three other toxic elements [3]. Due to that legislation, extensive research has been conducted world wide to develop lead free

solder[4-9]. The National Centre for Manufacturing Sciences (NCMS)[10] conducted a three year long study and evaluated over 79 potential alloy replacements. Based on their report, the International Electronics Manufacturing Initiative (iNEMI)[11] published a list of alloy recommendations for industries to follow. In that list, Sn alloys emerged as the material of choice because of its low melting point, manufacturability and reliability.

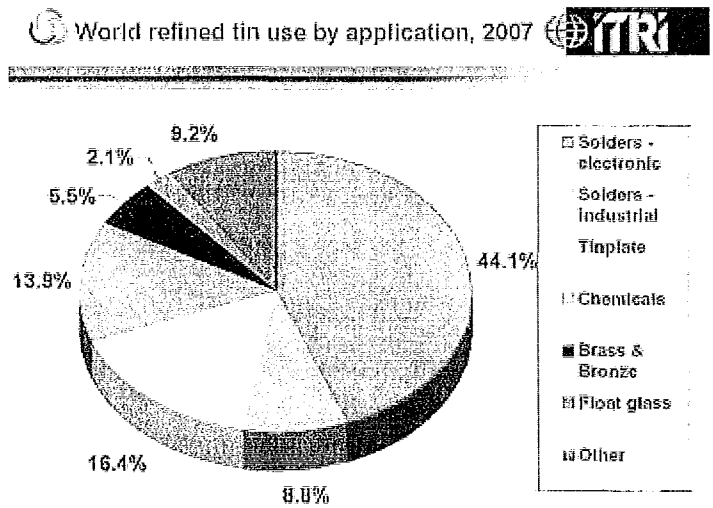

Figure 1. 1: Global Sn use in 2007 by market sector [1]

The non – toxic nature, superior corrosion resistance and attractive appearance have made Sn a very popular material for plating and surface finish. Over 90% of world production of tinplate is used to manufacture containers (tin cans) for packaging of food products and soft drinks, motor oil, disinfectants, detergents and polishes. Terneplate, which is mild steel coated with Sn-Pb alloy, offers strength, corrosion resistance and good thermal resistance. It is widely used as roofing and weather sealing material and in

construction of automotive gasoline tanks, signs and radiator header tanks [12]. A good number of other Sn alloys are also used in the automotive industry for hydraulic breaking mechanisms, disc brake pistons, piston rings where good resistance to wear and corrosion is required [12].

The organic and inorganic Sn chemicals account for almost half the total chemical usage in different industries. In petrochemicals, compounds of Sn find application in air purification systems, in binary oxide catalysts and reforming agents [2, 13]. Other potential fields of application have been identified in the next generation solar cells, in aerospace industries and in production of bio-diesels and hydrogen [13].

1.2 Microstructural Characteristics and Phase Structure of Sn

The industrial and commercial importance of Sn, as described in the previous section, is basically due to the wide range of its material properties that can be easily manipulated according to the user need by simple changes in some process parameters. It has been found that the structural, electronic and thermodynamic properties of Sn are very sensitive to temperature and pressure changes in the production process. Such sensitivity can be related to the position of Sn in the periodic table. Sn sits on the borderline between covalent and metallic bonding among group IV elements C, Si, Ge and Pb. Above Sn, the elements C, Si and Ge form a diamond cubic structure with directional covalent bonding while Pb, sitting below, forms an fcc structure with metallic bonding. This transitional behavior can be seen explicitly in the phase diagram of Sn.

Below 286 K, Sn possesses a diamond cubic structure with zero band gap [14]; this grey colored phase is also known as the α phase or the grey Sn. Above 286K, Sn crystallizes in a body centered tetragonal structure with two atoms per unit cell. This white colored metallic phase is also known as the β phase or the white Sn, which has a melting temperature of 505 K. The two crystal structures are illustrated in figure 1.2.

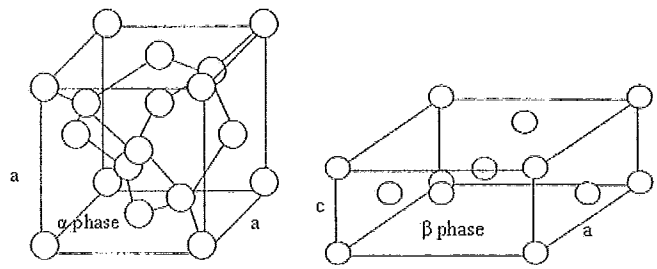

(i) (i i)

Figure 1. 2: Crystal structure of different phases of Sn. i) α phase or grey Sn
i i) β phase or white Sn.

The metallic β phase can be viewed as a distortion of the diamond cubic α phase. The transition between these two allotropes occurs at a temperature of 286K at atmospheric pressure which was given for the first time by Cohen and Van Lieshot [15]. There is a 27% volume change associated with this transition due to the difference in lattice parameters, which are: for β Sn, a = 5.831 Å and c = 3.181 Å, and for α Sn, a = 6.489 Å[16]. This transition, however, does not occur readily; β Sn has to be kept below this temperature for a sufficiently long time (days to years) before it can transform to α Sn. On the other hand, α Sn immediately starts to transform to β Sn after the temperature

has been raised to a few degrees above the transition temperature. The $\alpha \leftrightarrow \beta$ phase transition is mainly massive in nature, but partially proceeds by martensitic transformation [17].

1.3 Atomistic Simulation and Molecular Modeling: A Novel Approach

In recent years, atomistic simulations have proven to be quite effective in establishing quantitatively various material properties and processes [18-22]. The insights available through simulation of materials from the atomic level to the finite element level have significantly reduced wasted experiments, allowing a large number of candidate materials to be screened and processes to be optimized for a more efficient production. Molecular Dynamics simulation is one such technique, which is used to determine time dependent equilibrium and transport properties of a classical many body system. It solves the Newton's Law of motion $\mathbf{F}_i = m_i\mathbf{a}_i$ within any interacting system consisting i = 1....N particles. To study the evolution of the system with time, it is necessary to have a knowledge of the force acting upon each particle

1.3.1 Interatomic Potential

The interaction between two atoms or molecules in a system is the existing attractive or repulsive forces between them. The magnitude of that force is called the potential energy of that system. In order to accurately model any real alloy system, information about some physical parameters and equilibrium separation distance of the

two interacting species are used to determine the inter atomic potential. The parameters in the potential function are fitted to give desired properties of the materials such as cohesive energy, lattice parameters, elastic constants and vacancy formation energy, which are obtained from experiments or from first principle calculations. When an optimum fit is reached, that particular set of parameters is taken to represent the material in any further simulation operations.

An accurate model of the interaction energy or the potential of the system is critical for any theoretical or simulation work. The interaction between atoms will vary according to the type of material and the nature of the bonding. A single universal model can not describe all types of bonding. To date, quite a few methods have been published to model different types of materials. A Brief description of some of the major methods is given below.

(a) Lennard – Jones (LJ) Potential:

Atomistic simulation in earlier days employed a pair potential of the Lennard – Jones (LJ) type [23]. It is a simple mathematical model that can accurately approximate the non-bonded interactions existing between atoms or molecules separated by a short distance. LJ is valid for inert gases such as Ar, Xe. The potential resulting from the particle interaction is given by the following equation [24-26] –

$$V_{LJ} = 4\varepsilon\left[\left(\frac{\sigma}{r}\right)^{12} - \left(\frac{\sigma}{r}\right)^{6}\right] \qquad (1.1)$$

where σ is the finite distance at which the particles experience zero force, ε is the depth of the potential well and *r* is the distance between two particles. A plot of this function in figure 1.3 shows forces acting on such a potential system – a strongly repulsive short range interaction, attractive forces at large distances, and weak attractive forces at very large distance

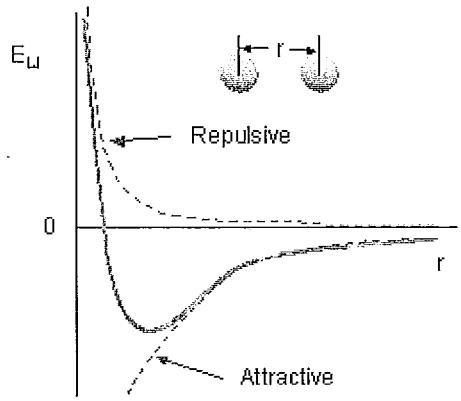

Figure 1. 3: Forces acting on a LJ system consisting of particles which are separated by a distance *r* [27]

Although this is an approximate potential, it has the features needed to describe the interactions between closed shell atoms and model "slip" along interatomic planes or the transformation of a solid to liquid when the particle motion increases with increasing kinetic energy [28-30], but it can not account for metallic and covalent bonding [31].

(b) Embedded Atom Method (EAM):

Daw and Baskes introduced the Embedded Atom Method (EAM) [32, 33] for calculating ground-state properties of realistic metal systems. It has enabled a semi –

quantitative and in some cases, even quantitative description of interatomic bonding in metallic systems. Based upon the Density Functional Theory (DFT) [34], this method produces different effective interactions between two atoms when they are in a different environment in a cluster. The energy of the system is given by –

$$E = \sum_i \left(F(\overline{\rho_i}) + \frac{1}{2} \sum \phi(r_{ij}) \right) \tag{1.2}$$

were $\varphi(r_{ij})$ is the pair potential term, $F(\rho_i)$ is the embedding function, r_{ij} is the distance between atoms i and j, ρ_i is the spherically averaged total electron density at atom i due to all other atoms in the system. Daw and Baskes published the EAM formulation for transition metals with fcc structure, which was later extended to metals with bcc crystal by Johnson and Adams [35, 36].

(c) Finnis – Sinclair (FS) Potential:

Another approach was proposed by Finnis – Sinclair [37] in 1984. They employed a semi empirical approximation of the DFT and derived a many body potential from the tight binding technique. The energy per atom at a given position is written as the sum of a N body term and a pair potential term –

$$U_i = U_N + U_P \tag{1.3}$$

The N body contribution is given by $U_N = -Af(\rho)$ where ρ is the local electronic charge density and the function f is chosen such that it mimics the tight binding theory. The core repulsion in equation 1.3 is given by $U_P = \frac{1}{2} \sum_{i \neq 0} V(r_i)$ where r_i is the interatomic

distance between atoms. This potential was originally developed for transition metals with bcc crystal structures but later Rosato et al. [38] extended it to transition metals with fcc lattices and Stutton and Chen [39] introduced variants for hcp transition metals.

(d) Modified Embedded Atom Method:

Though the EAM is widely used to describe late transition or noble metal systems, it can not account for the directional bonding in group IV elements like Sn. A modification to this method was proposed by Baskes et al [40] to include the angular forces resulting from directional bonding. The Modified Embedded Atom Method (MEAM) is basically an extension to the original EAM formulation which includes angular contributions to the interatomic force.

In MEAM, the total energy, E, of a system is also given by the form in equation 1.2. The embedding function is written in terms of a simple function of electron density and is given by

$$F(\overline{\rho}) = AE_c \frac{\overline{\rho}}{\rho_o} \ln(\frac{\overline{\rho}}{\rho_o}) \tag{1.4}$$

where, A is an adjustable parameter, E_c is the cohesive energy and ρ_0 is a density scaling parameter. The spherically symmetric electron density $\rho^{(0)}$ is used in the EAM to compute the average forces, but MEAM introduces angular forces through the angle dependent partial electron density $\overline{\rho}$,

$$\overline{\rho} = \frac{2\rho^{(0)}}{1+\exp^{-\Gamma}} \tag{1.5}$$

where, $\Gamma = \sum_{h=1}^{3} t^{(h)}(\rho^{(h)}/\rho^{(0)})^2$. The $t^{(h)}$ are constants and the $\rho^{(h)}$ term is the summation of atomic electron density that decay exponentially with separation distance r,

$$\rho^{a(h)}(r) = \exp[-\beta^{(h)}(r/r_e - 1)] \tag{1.6}$$

where the decay lengths $\beta^{(h)}$ are also constants and r_e is the nearest neighbor atomic distance.

The potential between two atoms separated by a distance r is given by [41]

$$\phi(r) = \frac{2}{Z}\{E^u(r) - F[\overline{\rho}^0(r)]\} \tag{1.7}$$

where Z is the number of first neighbors, $\overline{\rho}^0(r)$ is the background electron density of the reference structure which has $E^u(r)$ energy per atom. This energy is computed from the universal equation of state by Rose et al. [42]

$$E^u(r) = -E_c(1+a^*)\exp(-a^*) \tag{1.8}$$

where $\alpha^* = \alpha(\frac{r}{r_e} - 1)$ and $\alpha^2 = \frac{9\Omega B}{E_c}$ having Ω and B as atomic volume and bulk modulus respectively.

Accurately modeling Sn using classical interatomic potentials presents a significant challenge due to its complex crystal structure and allotropic transition. It is difficult to develop a single set of parameters which will model directional covalent bonding of α Sn and at the same time give fairly accurate interaction of metallic bonding of β Sn. The MEAM approach is usually employed in such a case as it includes the directional dependence of electron density and the resulting angular force.

1.4 Crystal – Melt Interface Properties and Its Influence on Growth Morphology

The solidification of crystals from the melt has been subjected to extensive study due to its importance from both the technological and industrial point of view. The final microstructure plays an important role in determining the quality of the end product in a wide range of solidification process [43-50]. Sn alloy solidification has been investigated thoroughly due to its important application in next generation lead free solder in electronic circuit boards. The integrity of the solder joint entirely depends upon the microstructure as it determines the sustainability of the joint under thermo-mechanical working conditions [51-55]. In most industrial processes, from casting to welding and soldering, the solidification mechanism follows a non – equilibrium path which gives rise to a branch like microstructure known as dendrites. The complex morphology of the dendritic microstructure, as illustrated in figure 1.4, determines the mechanical integrity of the solidified crystal.

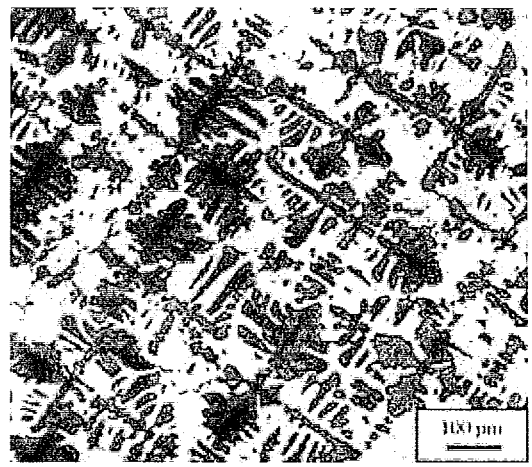

Figure 1. 4: Dendritic structure of multiphase Ni–21.9Al–8.1Cr–4.2Ta–0.9Mo–0.3Zr (at.%) intermetallic alloy [56]

Over the years, considerable effort has been directed towards the development of a theoretical understanding of dendritic solidification [57 – 62]. A major contribution came form Ivantsov [63] in the form of a solution to the problem of a steady state growing dendrite of parabolic shape under the assumption of an isothermal solid – liquid interface. It predicts that the product of the dendrite tip radius r times the tip speed V is a constant fixed by the degree of supercooling of the melt. The next major step was given by the advent of microscopic solvability theory of steady state dendrite growth [64]. It emphasizes the role of crystalline anisotropy on growth rate and tip radius of dendrites. The formation of the branch like morphology is strongly influenced by the anisotropy of the solid – liquid interfacial energy γ as well as on the anisotropy of the interface kinetic coefficient μ for larger growth rates. Later on, phase field simulation studies on dendritic

evolution [65 - 71] have further demonstrated an intimate link between mesoscale morphology of dendrites and the nano meter scale interface properties.

1.4.1 Crystal – Melt Interface Properties

There are two solid – liquid interface properties that govern the growth rate and morphological development in dendrite formation – the interfacial free energy γ which is given by the free energy per unit area required to create a interface between the crystal and its melt and the kinetic coefficient μ given by the proportionality constant between growth velocity and undercooling. The orientation dependence of these properties have a profound influence over the interface temperature. The equilibrium crystal – melt interface temperature during the solidification of a pure metal is given by the velocity dependent Gibbs – Thompson condition [72] –

$$T_I = T_M - \frac{T_M}{L}\sum_{i=1,2}\left[\gamma(\hat{n}) + \frac{\partial^2\gamma(\hat{n})}{\partial\theta_i^2}\right]\frac{1}{R_i} - \frac{V_n}{\mu(\hat{n})} \qquad (1.9)$$

where T_M is the melting temperature, L the latent heat of melting per unit volume. In the second term $\gamma(\hat{n})$ is the orientation dependent interfacial free energy where $\hat{n}$ represents the normal vector to the growth direction and θ_i refers to the angle between the growth direction and normal to the interface. This term represents the depression in the local temperature at an interface due to the interface characterized by the two principle radii of curvature R_i. A kinetic undercooling will also result from the growth velocity, V_n with a kinetic coefficient $\mu(\hat{n})$.

The orientation dependence of these properties will lower the interface temperature more in some specific orientation than the other. Such an imbalance will result in the breakdown of a planar interface and some orientation will experience faster growth resulting in branchlike dendritic structure. Therefore the final microstructure of the solidified crystal will depend upon the anisotropy of its solid – liquid interface properties.

1.4.2 Effect of Crystalline Anisotropy on Growth Morphology

The morphology of grown crystals arises from the underlying crystalline anisotropy, the fact that crystallographic properties depend upon orientation. Since the equilibrium shape of a solidifying crystal is the one which minimizes its interfacial free energy γ, the morphology of the growing crystal will be an image of its γ anisotropy [73-75]. But this anisotropy is characteristically very weak for dendrite forming systems with low entropy of melting and atomically rough interfaces. A precise value of this key parameter is difficult to compute or measure experimentally for metallic systems of practical relevance [76]. That is why the existing anisotropy measurements remain limited to a few transparent organic systems [77, 78]. In recent years, this difficulty has been overcome by computing the interfacial stiffness $\gamma + \gamma''$ which is an order of magnitude more anisotropic than γ itself [72, 79]. Figure 1.5 shows this difference of anisotropy of surface energy and surface stiffness. The figure (a) shows the surface energy plot of a Si surface and figure (b) is for stiffness of the same surface under same condition. This

figure, in principle, can also be used to understand the difference in interfacial energy and stiffness anisotropy.

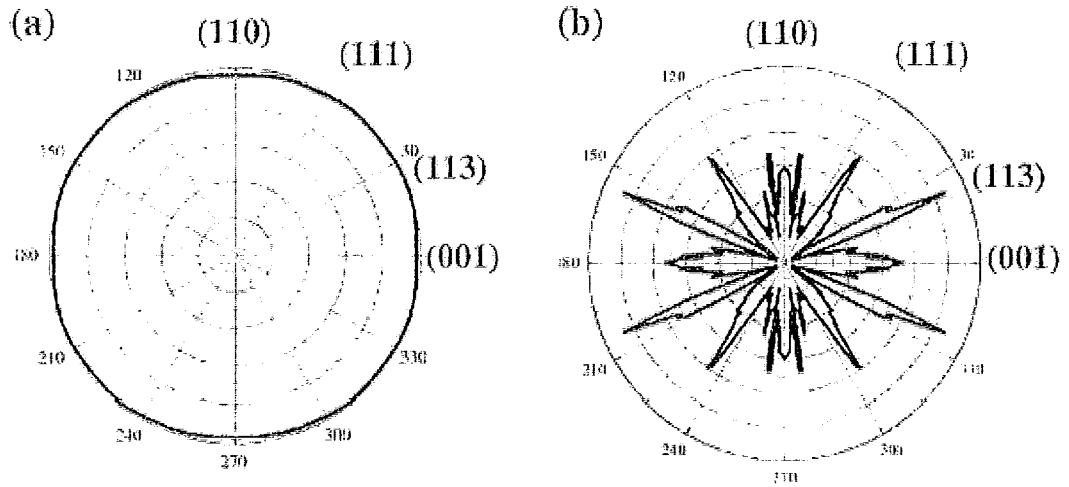

Figure 1. 5: Synthesis of the experimental results for Si shown as polar plot in the (110) plane. (a) Anisotropy of the surface free energy (gamma-plot), (b) anisotropy of the surface stiffness(stiffness-plot) [80].

Fundamentally, stiffness is the measure of the stability of the interface against undulation [80]. A high value of this key parameter infers that the interface will be more stable against any perturbations and it will require higher energy for the planer surface to breakdown. Anisotropy in stiffness will govern the height of fluctuations of the crystal – melt interface and in turn dendritic structure formation.

Over the last couple of decades, phase field models (PFM) have emerged as a powerful tool for modeling dendritic evolution starting from solidification of pure materials [81, 82] and later extending into alloy systems [83, 84]. These models have

benefitted by incorporation of the results of modeling at the atomic level. Atomistic simulation techniques like Molecular Dynamics (MD) and Monte Carlo (MC) have been developed to compute accurately the crystal – melt interface properties [72, 79, 85-88]. These simulation techniques have made it possible to quantify the diffuse interface and understand boundary conditions at the atomic level, which are then incorporated into PFM to solve dynamical problems. As it covers a wide range of length scale, the PFM has become the model of choice when it comes to modeling dendritic growth in solidifying systems.

1.5 Objectives of the Project

This research work is focused on developing a computational model for Sn and predicting the preferred orientation for growth of dendrites in a pure Sn system. The objectives of this project are –

(1) To develop a set of potential parameters for pure Sn and compute its structural, elastic and thermodynamical properties within acceptable accuracy. The parameters are optimized to simulate the equilibrium crystal – melt interface and to compute the solid – liquid interface properties.

(2) To compute the interfacial stiffness of the crystal – melt interface of a pure Sn system and determine the equilibrium shape of a solidifying crystal. The Wulff plot of a

single Sn crystal will provide the underlying physics of the interface and anisotropy of the crystal melt interfacial energy.

(3) To determine the kinetic coefficient of the interface growth of a pure Sn system and its variation with orientation.

The rest of this thesis is organized as follows. The subsequent chapter will present a review of an existing Sn MEAM potential due to Ravelo and Baskes [89] and will evaluate the phase equilibrium behavior of the two crystal phases α and β and the liquid phase. Simulation techniques are detailed for the computation of specific properties and compared with the result of the existing potential. A method is presented to modify the potential to improve upon the melting properties and correct the stability of phases. Then chapter 3 describes in detail the anisotropic free energy computation and the determination of the equilibrium shape of solidifying crystal by constructing the Wulff plot. Chapter 4 describes simulation methods to determine the orientation dependent kinetic coefficient and interface mobility. The final section will summarize the research work and will suggest future work for further improvement.

CHAPTER 2

Inter – atomic Potential Computation

2.1 Overview of Sn Potential

It is not always possible to develop a single classical potential that describes the interactions of certain systems in all chemical environments. This transferability problem is particularly severe in the case of materials for which little experimental data is available. To date very few classical interatomic potentials for Sn have been developed due to this problem. Berroukche et. al. [90] published a set of potential parameters for Sn using the three-body potential of Tersoff [91] which is an empirical interatomic potential system used to determine the interactions in complex covalent systems. They performed MD computations of the temperature dependent structural and thermodynamic properties of α Sn but could not extend their study beyond the transition temperature. The chosen potential system limits the system to α phase of Sn only, can not account for the metallic bonding responsible for the body centered tetragonal phase β Sn.

Ravelo and Baskes [89] chose the modified version of the embedded atom method (MEAM) [92] formulation to represent the atomic interactions in Sn. As shown in the previous chapter, MEAM includes the directional bonding of the covalently bonded

systems and it can as well be used to set up metallic material by assuming a spherically averaged electron density. This type of potential system can ideally be used to model Sn. Ravelo and Baskes published a set of MEAM parameters for Sn by fitting to the cohesive energy, lattice and elastic constants of α Sn, the lattice constants and vacancy formation energy of β Sn and the energy difference between various forms of Sn at 0K. Their potential, given in Table 2.1, hereafter will be referred as the RB potential.

Table 2. 1: MEAM parameters of Sn developed by Ravelo and Baskes.

Potential	Ec	A	r^0	α	$\beta^{(0)}$	$\beta^{(1)}$	$\beta^{(2)}$	$\beta^{(3)}$	$t^{(1)}$	$t^{(2)}$	$t^{(3)}$
RB	3.08	1	1	6.20	6.20	6.0	6.0	6.0	4.5	6.5	-0.183

This research work will also follow the MEAM formulation to model atomic interaction in Sn and to compute its different structural, thermodynamic and elastic properties.

2.2 Evaluation of RB Potential

The RB potential is first evaluated for its general applicability; that is whether it can be actually used to model the thermodynamic and kinetic properties of the solid – liquid interface of the two phases of Sn. The RB parameters are used to set up a Sn system using LAMMPS code [93] and a few of its properties are computed. If those properties are found to be within an acceptable error margin, then it can be accepted as a

general Sn potential. Computational details of Sn properties are given in the following sections.

2.2.1 Lattice parameter computation

Lattice parameter or lattice constants are the equilibrium distance between two atoms in a unit cell of a crystal lattice. The α Sn has a diamond cube structure, so there will be only one lattice parameter ***a*** required generate a periodic α Sn crystal. On the other hand, β Sn has a tetragonal unit cell structure that requires two parameters ***a*** and ***c*** to be defined. These parameters will also change with temperature; higher temperature will create higher vibration within the crystal resulting in an increase of the distance between atoms.

Lattice parameters of α and β Sn were computed using a Nose – Hoover style isothermal – isobaric ensemble (NPT) with pressures in all three dimensions set to zero. Equilibrating a β Sn system consisting of 8×8×32 unit cells and 12,288 atoms at different temperatures, the total length of the box was measured under the zero pressure condition. Dividing the total length in any direction by the number of unit cells in that direction, the lattice constant at that temperature was measured. Figure 2.1 (a) (b) shows the trend in change of lattice parameter with temperature. Similar result was found in the experiment of α Sn.

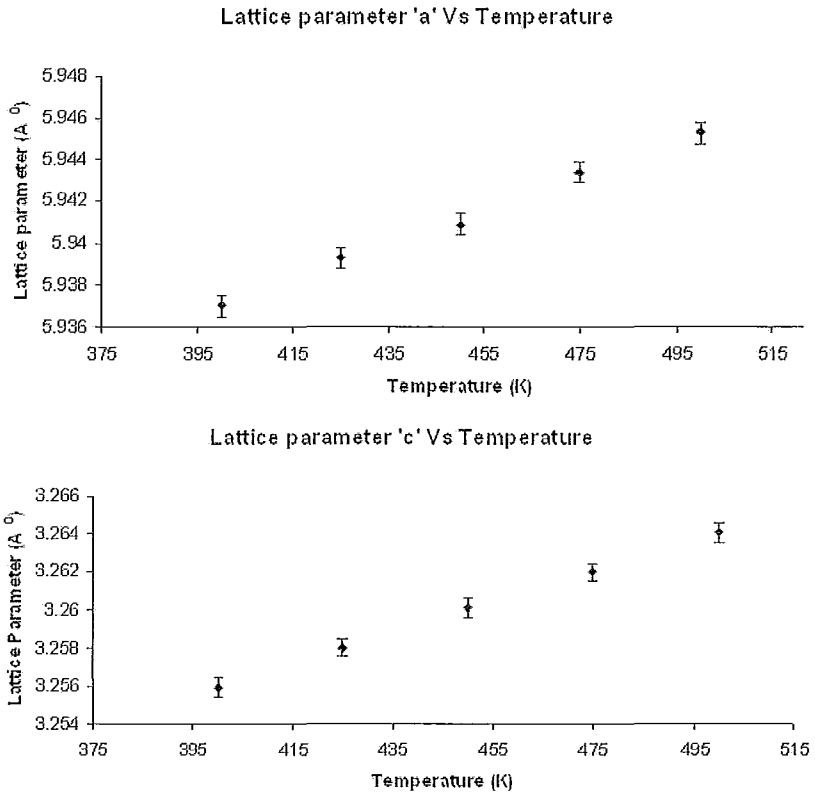

Figure 2. 1: Change in lattice parameter of β Sn at different temperatures.

It can be noted from figure 2.2 that the ratio of the two lattice parameters for β Sn remains almost the same for all the temperatures.

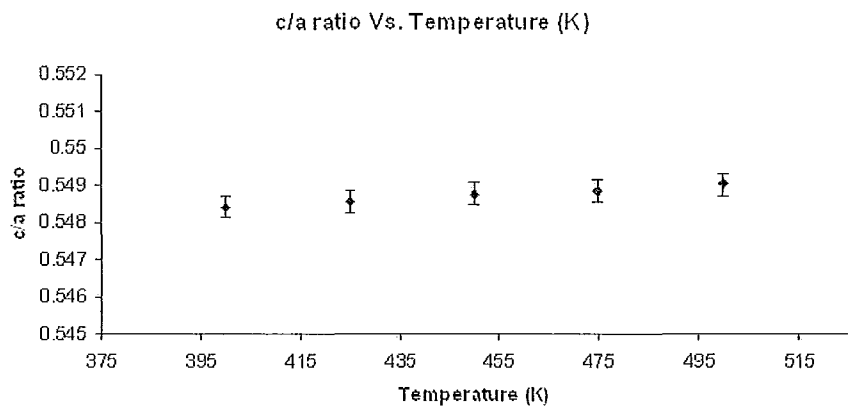

Figure 2. 2: Ratio of the two lattice parameters of β Sn

The linear thermal expansion coefficient is given by the following relation [94] –

$$\alpha(\Delta T) = \frac{\Delta L}{L_0 \Delta T} \tag{2.1}$$

Applying this relation on the ***a*** lattice parameter of β phase of Sn generated using the RB potential, the linear thermal expansion coefficient $\alpha(\Delta T)$ was found to be 13.96 $\times 10^{-6}$ K^{-1} at 300 K, whereas in literature it is found to be 23.5 $\times 10^{-6}$ K^{-1} [94].

The trend of result in this work was found to be pretty consistent with lattice parameter published in the RB paper, which were for α Sn ***a*** = 6.483 and for β Sn ***a*** = 5.92 and the ***c/a*** ratio of 0.546.

2.2.2 Ground state energy computation

The ground state energy of a system is referred to the energy at absolute zero temperature and at zero entropy. In this lowest energy state, the atoms will be sitting on a perfect crystalline lattice.

In this work, the ground state energy was computed through the LAMMPS energy minimization command, which performs an energy minimization by iteratively adjusting atom coordinates using a conjugate gradient scheme. The total potential energy of the system is minimized here, which is given as a function of the N atom coordinates:

$$E(r_1, r_2, \ldots, r_N) = \sum_{ij} E_{pair}(r_i, r_j) + \sum_{ij} E_{bond}(r_i, r_j) + \sum_{ijkl} E_{angle}(r_i, r_j, r_k) +$$

$$+ \sum_{ijkl} E_{dihedral}(r_i, r_j, r_k, r_l) + \sum_{ijkl} E_{improper}(r_i, r_j, r_k, r_l) + \sum_{i} E_{fix}(r_i) \qquad (2.2)$$

The first term in the equation is the sum of all non-bonded pairwise interactions, the rest of the term are bond, angle, dihedral, and improper interactions respectively, and energy due to additional operations in the system which can act as constraints or apply force to atoms. In this experiment, no additional fixes were applied on the system, so the energy function excluded the last term. The starting point for the minimization is the current configuration of the atoms and progresses by iterating atom co-ordinates and evaluating energy at each iteration step. It will stop if the energy tolerance, defined as the ratio between the energy difference at successive iterations and the energy magnitude, is equal to the value set during the simulation run, 1.0e-4 for this computation.

The ground state energies as computed from this computation were, for α Sn -3.1396 eV/atom and for β Sn -3.085 eV/atom. Comparing this result with the RB paper and other published literature, it was found to be consistent with both RB and other experiments.

2.2.3 Melting point determination

Computation of the melting point (T_M) is a two step process. The first step in accurate determination of T_M is an approximate estimation by extrapolating the solid –

liquid interface velocity versus temperature plot to the point where the velocity is zero. The second step consists of the co – existence approach [96] that improves on the uncertainty of T_M.

In the first step, Molecular Dynamics (MD) simulations are performed on systems containing both solid and liquid phases in an NP_zAT ensemble at various trial temperatures near the experimental T_M. The total number of atoms is kept fixed in a system with a fixed cross sectional area A; only the direction normal to the interface (along z) is allowed to change through out the simulation in order to maintain the isobaric condition (P = 0). The growth velocity of the moving interface is monitored by the change in the potential energy of the entire system over the course of simulation at each temperature. This change is indicated by the slope of the potential energy versus time plot. The approximate melting point is obtained by extrapolating the temperature to the point where there will be zero velocity of the interface; that is the slope of the potential energy curve will be nearly zero. Below this temperature, the crystal part of the system will grow at the expense of the liquid while above this temperature some of the solid will melt which will create a velocity of the crystal – melt interface. At the melting point, if any fluctuation at the interface results in solidification of some portion of the liquid, it will immediately melt back to maintain the equilibrium. As a result, the crystal – melt interface will remain stationary. But due to the noise at the fluctuating interface, this method will have some uncertainties in its results.

In the present work, a β Sn system consisting of 8×8×32 unit cells and 12,288 atoms was set up using the RB potential. The NP_zAT ensemble is applied at different trial temperatures of 415 K, 420 K, 425 K, 430 K and 435 K and the velocity of the solid - liquid interface was monitored by the change in potential energy with time. Figure – 2.3 shows the potential energy - time plot for this Sn system at three temperatures giving an idea about the interface velocity. This computation was conducted on two orientation of the crystal – melt interface, which were (001)[100] and (110)[$1\bar{1}0$].

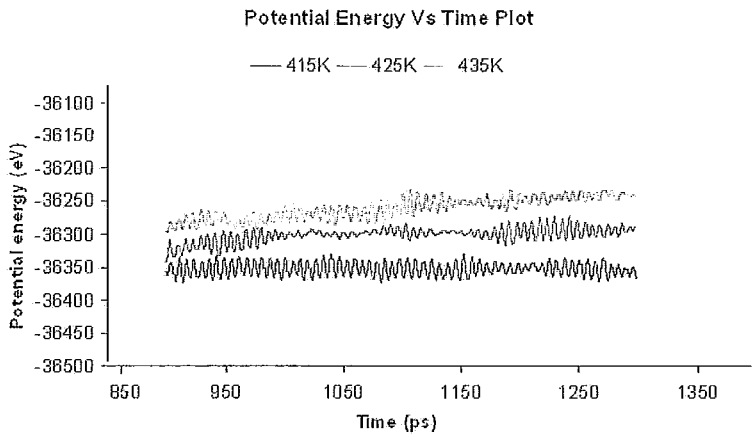

Figure 2. 3: Potential energy versus time plot of the β Sn system in (110)[$1\bar{1}0$] direction at different trial temperatures.

Plotting the slope of these curves with temperature will result in figure 2.4 (a) and (b) and extrapolating the slope to zero gives the first approximation of the melting point as 415 ± 3 K.

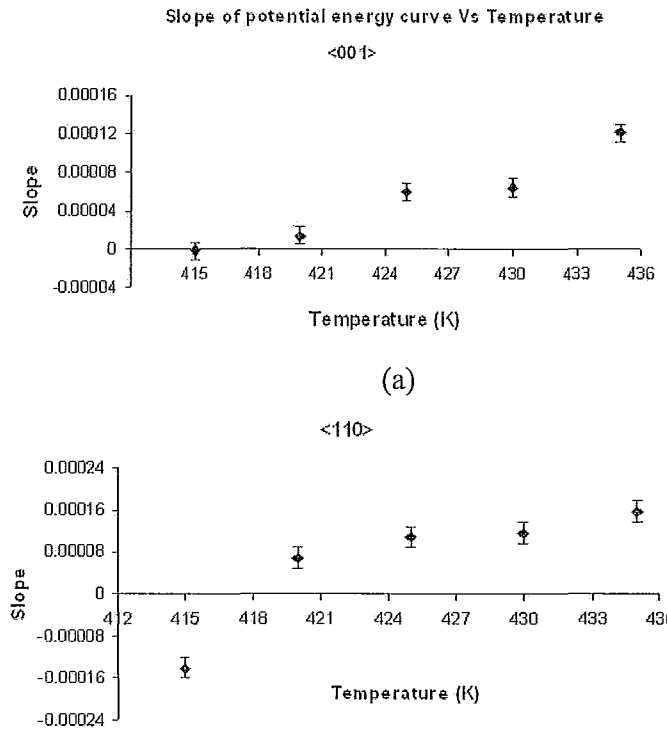

Figure 2. 4: Slope of potential energy – time curve with respective temperature

(a) (001)[100] (b) (110)[$1\bar{1}0$]

In the second step of the melting point determination, a co-existence approach [96] is applied. This requires a MD simulation to run in a micro canonical (NVE) ensemble on a solid – liquid system at the melting temperature approximated from the first step. This approach is based on the principle that if the solid – liquid system is at equilibrium, then the temperature of the system will be at the melting point. If the system goes below its melting point then some of the liquid will solidify to conserve the total energy, resulting in release of latent heat into the closed system. This latent heat will increase the

temperature towards the equilibrium melting point. Similarly, if the temperature goes above the melting point, some solid will melt absorbing some heat from the system and will lower the temperature towards its melting point. The pressure of the system will also equilibrate and the system will evolve towards equilibrium.

In this work, the NVE ensemble was applied on a system similar to the one mentioned in the first step. The temperature of the experiment was taken to be 415K as determined in the first step. The change in temperature was monitored over time and it was found that over a time span of 3 ns, there was not much change in the temperature of the system. This reconfirms the approximation of the first step that the melting point of the RB Sn system was 415 ± 3 K.

Comparing the result of this work with those of the RB and other published literature, a huge difference is found between the established melting point for Sn (505 K) and that of this work (415 ± 3 K). The RB predicts a melting point of 453 K with a ±50 K error margin which is due to error in its computation of the free energy of liquid. The result of this work falls within that error margin of RB and can be considered as a reasonable reproduction of RB result.

2.2.4 Gibbs Free Energy Plot

To determine the free energy difference between two phases in an atomistic simulation a reference state must first be determined. Although several studies have

utilized, for example, a quasi-harmonic model for the free energy of the crystal at low temperatures [97,98], recent investigations [99,100] have shown that the melting point, where the free energy of the solid and liquid are equivalent, can be used as a convenient reference temperature.

The free energy as a function of temperature can be found from the following thermodynamic relationship [99]:

$$\frac{\mu^S - \mu^L}{T} = \int_T^{T_M} \frac{H^S(T') - H^L(T')}{T'^2} dT' \tag{2.3}$$

where H represents the enthalpy and the superscripts S and L refer to the solid and liquid phases respectively. Over a wide temperature range the approximation $\mu^S - \mu^L = L(T\text{-}T_M) / T_M$ where L is the latent heat, was found to be very accurate and the results presented in this research work have utilized the simple approximation.

Latent heat can be defined as the difference in potential energy between the solid and liquid phase at the melting point. To compute this energy, a β Sn system consisting of 8×8×32 unit cells and 12,288 atoms was set up using the RB potential at 415 K. Potential energy per atom was recorded for the system at both crystalline and liquid state. The latent heat was computed as 0.032 eV/atom, the same as published in the RB paper, which is considerably lower than the experimental value of 0.073 eV/atom [96].

The free energy of the crystal phase minus that of the liquid as a function of temperature is plotted in figure 2.5. The data points indicated by the circles refer to the grey Sn phase and the squares denote the thermodynamic behavior of the white Sn phase. The results illustrate a main weakness of the RB potential; it predicts that the grey Sn phase is always more stable than the β phase whereas experimentally there is range of temperatures where β is the lowest free energy phase. The free energies of α and β become equivalent only at a very high temperature, roughly 600K, which is above the melting point of either crystal. It can be concluded that the RB potential can not predict the correct stability of phases in a pure Sn system.

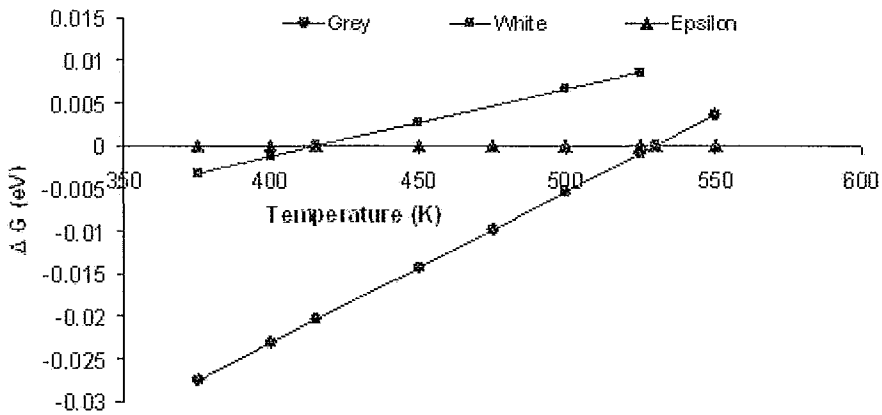

Figure 2. 5: Change in Gibbs free energy with temperature for α and β phases of Sn. ΔG is the free energy of the crystal minus that of the liquid

2.2.5 Solidification of a single crystal of Sn

An additional complication was uncovered when attempting to model the β phase-liquid interface using the RB potential. A β Sn system of 30×30×12 dimension, consisting of 64,800 atoms, was at first equilibrated at a temperature of 387K. Keeping a region in the middle of the system in the solid β phase state, the rest was melted at 800K. When the temperature of the whole system was lowered to 387 K in 3 ns, with time steps of 1 fs, to grow a single crystal of white β phase from its melt, the system solidified as a poly crystal with a different crystal geometry than the parent phase as shown in figure 2.6 However the phase that formed at the original β-liquid interface was neither α or β. The new phase, which will be referred to as the ε phase, has a body centered tetragonal crystal structure with two atoms per unit cell and dimensions of a = 5.18 Å and c = 3.32 Å at 1K. The formation of ε, which is not observed experimentally, appears to be closely related to the specific crystallographic orientation of the solid-liquid interface. As shown in figure 2.6, the ε readily forms at the 100 interface of β, but is not observed for other crystal-melt faces.

However, the ε phase may be related to the transition between pressure induced phase changes mentioned in some literatures [101-106]. The free energy of the new phase is plotted in figure 2.5 and it can be seen that it is very close in value to the liquid free energy over a wide temperature range.

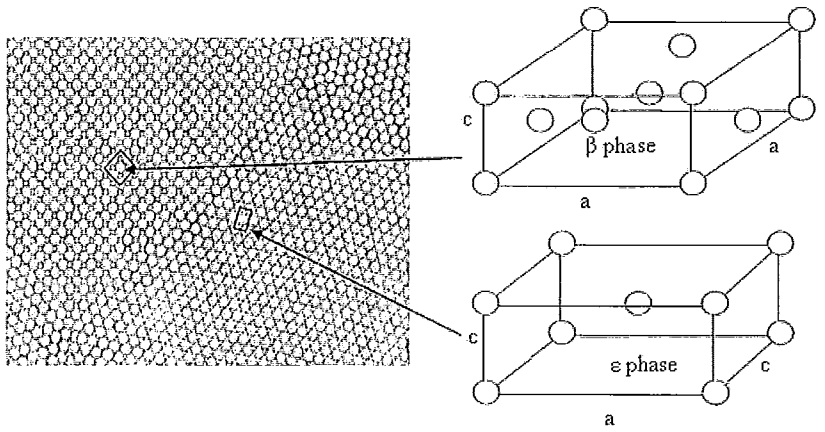

Figure 2. 6: Unit cells of the β and ε phase resulting from the RB potential. The ε phase, which is not observed experimentally, forms at the β solid – liquid interface.

Analyzing the results of phase equilibrium obtained from the RB potential, it can be concluded that this potential is not ideal for simulating the crystal – melt interface in Sn. This model raises some thermodynamic issues not found in the real metal. Therefore, this work proposes some modifications of this RB potential, which are detailed in the following sections.

2.3 Modification of the RB potential

As it has already been discussed in the previous sections, the properties of the Sn model will depend upon the potential parameters which will establish the interaction between atoms. Modification of the Sn model refers to changes in those parameters which will optimize the properties. To modify this potential, six Sn MEAM parameters of the RB potential were targeted. The chosen parameters were A, $\beta^{(o)}$, $t^{(1)}$, $t^{(2)}$, $t^{(3)}$ and the

parameter β where $\beta = \beta^{(1)} = \beta^{(2)} = \beta^{(3)}$. A small change in any of the six target parameters will vary all of the resulting materials properties of the MEAM Sn. The properties chosen to be evaluated were lattice parameter ***a*** of α Sn, lattice parameter ***a*** and ***c*** of β Sn and their ground state energies. To assess the property changes a series of simulations were performed where one parameter is altered by a small (approximately 5%) amount and the resulting property changes were computed. For example, by changing the parameter A, the associated change in lattice constant of the α phase is computed according to the relation –

$$\frac{\partial a_\alpha}{\partial A} = \frac{a_{\alpha,SnX} - a_{\alpha,RB}}{A_{SnX} - A_{RB}} \tag{2.4}$$

where SnX denotes the new set of MEAM parameters.

In order to formulate a Sn potential with improved melting and α→β transition temperatures, it can be noted that the ground state energy of the α Sn must be increased and the cohesive energy of the β Sn phase should be decreased (see figure 2.5). In addition, to prevent the formation of the non-equilibrium ε phase its cohesive should be increased. Finally, the original RB potential predicts lattice parameters for the two equilibrium crystal phases, ie. a_β, c_β and a_α, in perfect agreement with experiment and therefore the modification scheme should result in no change from the RB result.

Changes in the six materials parameters just described are related to the six target MEAM parameters by the following six by six matrix:

$$\begin{bmatrix} \partial a_\alpha \\ \partial a_\beta \\ \partial c_\beta \\ \partial E_\alpha^0 \\ \partial E_\beta^0 \\ \partial E_\varepsilon^0 \end{bmatrix} = \begin{bmatrix} \frac{\partial a_\alpha}{\partial A} & \frac{\partial a_\alpha}{\partial \beta^0} & \cdots & \cdots & \cdots & \frac{\partial a_\alpha}{\partial t^3} \\ \cdots & \cdots & \cdots & \cdots & \cdots & \cdots \\ \cdots & \cdots & \cdots & \cdots & \cdots & \cdots \\ \cdots & \cdots & \cdots & \cdots & \cdots & \cdots \\ \cdots & \cdots & \cdots & \cdots & \cdots & \cdots \\ \frac{\partial E_\varepsilon^0}{\partial A} & \cdots & \cdots & \cdots & \cdots & \frac{\partial E_\varepsilon^0}{\partial t^3} \end{bmatrix} \begin{bmatrix} \partial A \\ \partial \beta^0 \\ \partial \beta \\ \partial t^1 \\ \partial t^2 \\ \partial t^3 \end{bmatrix}$$

The matrix is then inverted to obtain any desired change in the properties. The parameters $\beta^{(1)}$,$\beta^{(2)}$ and $\beta^{(3)}$ were later varied to get a better approximation of lattice constants. The new set of MEAM parameters is given in table 2.2; which, hereafter, will be referred to as the Sn29 potential.

Table 2. 2: New set of MEAM parameters for Sn

Potentia	Ec	A	r^0	α	$\beta^{(0)}$	$\beta^{(1)}$	$\beta^{(2)}$	$\beta^{(3)}$	$t^{(1)}$	$t^{(2)}$	$t^{(3)}$
Sn29	3.08	1.0386	1	6.20	5.945	6.0	6.0	5.7	4.5	6.5	-0.183

2.4 Evaluation of Sn29 potential

Similar to the process followed in evaluating RB potential, Sn29 was also subjected to scrutiny. Structural, thermodynamic and elastic properties are computed for a Sn system generated using Sn 29 and compared with published literature. A brief description of the computational details is given in the following.

2.4.1 Structural property computation

Structural properties of any material include its lattice constants and ground state energies. Methods of computation of these properties have been detailed in section 2.2.1 and 2.2.2, so it will not be repeated here. Following those procedures, the ground state values of the cohesive energies and the lattice parameters for the Sn29 potential are computed and summarized in table 2.3. Also provided is a comparison with experiment and the RB predictions. In all cases there is excellent agreement with experiment. The main deviation occurs in the *c/a* ratio of the β phase, but this parameter is still within 1% of the experimental value. There was improvement on the value of linear thermal expansion coefficient $\alpha(\Delta T)$.

Table 2. 3: Structural properties of Sn computed from the new potential

Properties	From literature	RB potential	Sn29
E_{coh} (Grey Sn) (eV/atom)	-3.14[107]	-3.140	-3.109
E_{coh} (White Sn) (eV/atom)	-3.10[103]	-3.085	-3.086
a_α (Å)	6.483[108]	6.483	6.555
a_β(Å)	5.8313[108]	5.92	5.916
c_β(Å)	3.188[108]	3.232	3.261
c/a ratio	0.546[108]	0.546	0.552
$\alpha(\Delta T)$ K^{-1}	23.5×10^{-6} [95]	13.96×10^{-6}	19.19×10^{-6}

2.4.2 Thermodynamic property computation

The melting point was computed for this new set of Sn parameters following the procedure described in section 2.2.3. For Sn29, the melting point was found to be 547 ± 3K, which is still within a ± 50K range from the experimentally established melting point of 505K. Figure 2.7 shows the free energy plot for the α, β and ε phases using Sn29. The improvement over the results of figure 2.5 is clear. Now the white tin phase is stable with respect to grey Sn over a temperature range in good agreement with experiment. An extrapolation of the α and β free energy curves results in a transition temperature between the two, which is 275K. It is in excellent agreement with the 286K value found in experiment.

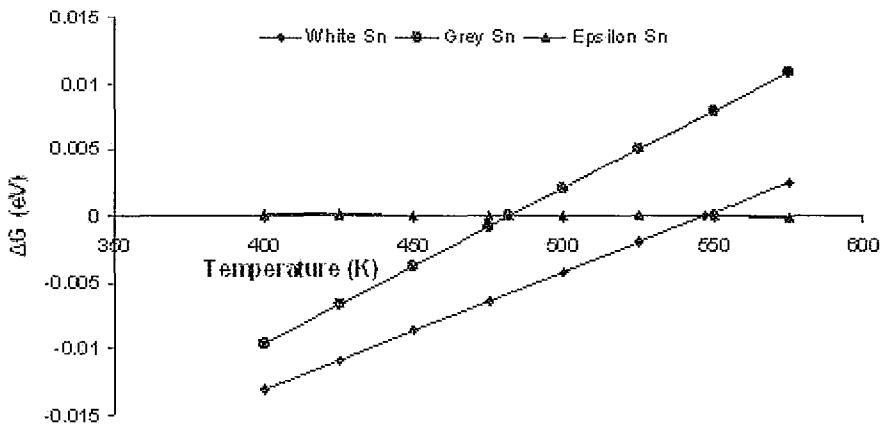

Figure 2. 7: Change in Gibbs free energy with temperature for the white, grey and epsilon phases of Sn for the potential Sn29

The transition temperatures are summarized in table 2.4. Also evident from the table is the fact that the improvement in equilibrium transition temperatures also results

in a considerable improvement in the latent heats of transitions. The latent heat of the $\alpha \rightarrow \beta$ transformation (.022 eV/atom) predicted by the Sn29 potential is in agreement with experiment. The latent heat of melting is considerably lower than the actual value, but is much closer than the RB result.

Table 2. 4: Thermodynamic properties as computed for Sn29. The subscript t refers to the α– β transition and 'm' refers to the melting of β Sn.

Property	From Literature	RB potential	Sn29
T_t (K)	286	286	275
T_m (K)	505	453 ± 50	547 ± 3
H_t (eV/atom)	0.022[109]	0.056	0.022
H_m (ev/atom)	0.073[109]	0.032	0.0486

In addition the Sn29 interatomic potential represents an improvement over the RB potential with respect to the ε phase. The experiment with the single crystal solidification, as detailed in section 2.2.5, was repeated with Sn 29 and the formation of ε at the β-liquid interface was no longer observed.

2.4.3 Elastic property computation

The elastic properties of a system determine how stress and strain are related. An elastic constant tensor c_{ijkl} is defined to establish this relation which is given by Hook's Law -

$$\sigma_{ij} = c_{ijkl}\varepsilon_{kl} \tag{2.5}$$

where σ_{ij} is the stress and ε_{kl} is the strain. For anisotropic material, this relation can be written in detailed form given in the following –

$$\begin{aligned}
\sigma_{xx} &= C_{11}\varepsilon_{xx} + C_{12}\varepsilon_{yy} + C_{13}\varepsilon_{zz} + C_{14}\varepsilon_{xy} + C_{15}\varepsilon_{xz} + C_{16}\varepsilon_{yz} \\
\sigma_{yy} &= C_{21}\varepsilon_{xx} + C_{22}\varepsilon_{yy} + C_{23}\varepsilon_{zz} + C_{24}\varepsilon_{xy} + C_{25}\varepsilon_{xz} + C_{26}\varepsilon_{yz} \\
\sigma_{zz} &= C_{31}\varepsilon_{xx} + C_{32}\varepsilon_{yy} + C_{33}\varepsilon_{zz} + C_{34}\varepsilon_{xy} + C_{35}\varepsilon_{xz} + C_{36}\varepsilon_{yz} \\
\sigma_{xy} &= C_{41}\varepsilon_{xx} + C_{42}\varepsilon_{yy} + C_{43}\varepsilon_{zz} + C_{44}\varepsilon_{xy} + C_{45}\varepsilon_{xz} + C_{46}\varepsilon_{yz} \\
\sigma_{xz} &= C_{51}\varepsilon_{xx} + C_{52}\varepsilon_{yy} + C_{53}\varepsilon_{zz} + C_{54}\varepsilon_{xy} + C_{55}\varepsilon_{xz} + C_{56}\varepsilon_{yz} \\
\sigma_{yz} &= C_{61}\varepsilon_{xx} + C_{62}\varepsilon_{yy} + C_{63}\varepsilon_{zz} + C_{64}\varepsilon_{xy} + C_{65}\varepsilon_{xz} + C_{66}\varepsilon_{yz}
\end{aligned}$$

The solutions to these equations do not require a specification of all 36 of these constants, the number of independent C terms can be reduced by considering crystal symmetry and crystal structures.

The components of the 6 × 6 elastic constant matrix are computed by the partial derivative of the stress tensor with respect to deformation [110] –

$$C_{ijkl} = \frac{\partial \sigma_{ij}}{\partial \varepsilon_{kl}}\Big|_{T,\varepsilon(kl)} \tag{2.6}$$

According to a procedure described by Clancy et al [110], to compute these elastic constants, a uniaxial tensile deformation is applied in the [100] direction of the periodic

boundary cell in a constant volume – temperature (NVT) ensemble; the other two directions are kept fixed. In this work, a 8×8×32 unit cells system of β Sn containing 12,288 atoms at 1K temperature was used to conduct this experiment. A 5% tensile deformation was applied over a simulation period of 2ns with a relative deformation rate of 1×10^{6} s^{-1} or 9.946×10^{-5} Å /ps and the stress tensor was recorded at a time interval of 1fs. As indicated in the stress tensor equation, the slope of a given component of the stress tensor plot vs the corresponding relative deformation will yield the elastic constant in that direction. For example, for a deformation in x, the slope of the stress tensor τ_{xx} and relative deformation ε_{xx} plot will give the elastic constant C_{11}. Table 2.5 lists the elastic properties of the stable phases.

Table 2. 5: Elastic properties as computed for Sn29. All the computation are done at 1K temperature

Quantity	β (RB)	β (from literature)	β (Sn29)	α (RB)	α (from literature)	α (Sn29)
B (eV /Å^3)	0.40	0.356 [95]	0.392	0.263	0.266[95]	0.264
C_{11} (eV /Å^3)	0.683	0.458[95]	1.105	0.458	0.431[95]	0.418
C_{33} (eV /Å^3)	0.673	0.566[95]	0.683	…	…	…
C_{12}(eV /Å^3)	0.360	0.374[95]	0.161	0.166	0.133[95]	0.182
C_{13} (eV /Å^3)	0.217	0.244[95]	0.246	…	…	…

The elastic properties represent the main weakness of the current potential. The values of C_{11}, C_{12} and C_{33} vary from both experiment and the RB prediction. Moreover, experimentally and also in the RB potential, it is found that $C_{12} > C_{13}$, but Sn29 shows the opposite trend.

The bulk modulus can be calculated by estimating the change in dimension due to the change in hydrostatic pressure on the system [101]. If a pressure ΔP induces a change of volume ΔV, then the bulk modulus B is given by –

$$B = \frac{\Delta P}{(\Delta V / V_0)} \tag{2.7}$$

where V_0 is the initial volume of the system. 1bar was used as the reference state for this experiment and 1000bar as the new state on a 8×8×32 unit cells system of β Sn containing 12,288 atoms at 1K temperature. For the experiment on α Sn, the same condition was applied on an 8×8×8 unit cells system containing 4096 atoms at 1K temperature. Comparing the experimental results with literature, it can be seen from table 5 that it is pretty much consistent with published results.

It can be concluded from the experiments and results detailed in this chapter that the new potential Sn29 offers considerable improvement over the previous RB potential in terms of the phase equilibrium characteristics, the α→β transition temperature, the melting point and the latent heats of transformation. This new potential can be used to model the crystal – melt interface and compute the interface properties to understand the dendrite growth direction in Sn.

CHAPTER 3

Interfacial Stiffness and Interfacial Free Energy Computation

3.1 Complexities in Experimental Measurement of Interfacial Free Energy (γ)

The solid – liquid interfacial free energy (γ) has an important influence on the microstructural morphologies of a crystal growing from its melt. The underlying crystalline anisotropy guides the pattern formation in dendritic solidification by preventing the growing tips of primary and higher order dendrite branches from splitting. In most of the commercially important materials, the anisotropy in γ is usually on the order of 1 – 2 % which makes it very difficult to measure experimentally or computed.

One of the earliest experiments to determine γ was conducted by Turnbull [112] in 1950. The interface energy was estimated from the nucleation kinetics using the classical nucleation technique. But this estimation could not explain the orientation dependence as the calculated value was orientationally averaged and also, the measured nucleation frequencies were in error by a factor ~ 10^4.

Gündüz and Hunt [113] introduced an experimental method for determining γ from the shape of a grain boundary groove (GBG). The shape of grain boundary cusps was

measured after annealing in a temperature gradient and rapidly quenching to preserve the shape. This technique is based on the direct application of the Gibbs–Thomson equation, which is given as [114] :

$$\Gamma = r\Delta T_r = \frac{\gamma_{SL}}{\Delta S_f} \tag{3.1}$$

where, Γ is the Gibbs–Thomson coefficient, r is the radius of curvature, ΔT_r is the curvature undercooling, and ΔS_f is the entropy of fusion per unit volume. The GBG technique employs a finite difference model to determine the Gibbs–Thomson coefficient. But accurately measuring the curvature of grain boundaries of opaque materials presents a challenge in itself. Due to this inherent difficulty associated to this experiment, only a handful of transparent materials have been subjected to study [115-117]. This method, also, does not take into account the crystalline anisotropy.

Recently, Napolitano et al. [118,119] developed a quantitative method for measuring the interfacial energy through an equilibrium shape measurement. They applied the Wulff theorem on the crystal – melt interface of Al-Cu and an Al-Si alloy. According to this theory, the relationship between the interfacial energy function, γ *(n)*, and the equilibrium shape of a droplet, *r (n)*, embedded within a continuous second phase is given by –

$$\frac{\gamma_1}{\gamma_2} = \frac{r_1}{r_2} \tag{3.2}$$

where the subscripts indicate two arbitrary crystallographic directions. The equilibrium shape of the solidifying crystal can be determined from the function $\gamma(\theta)$, known as the γ -plot. This method could provide a good estimate of the anisotropy of the interfacial energy anisotropy for the materials used in the study. Though it paved the way for understanding the crystal morphology, it could not measure the magnitude of the interfacial free energy γ.

Though an important commercial material, not many research works have been conducted on pure Sn to understand its morphological development and the effect of crystal – melt interfacial energies and associated anisotropies. Esin et al.[121] studied the crystallographic orientation of dendrites developing on the surface of a supercooled melt of pure Sn. They conducted the experiment in the range of 0 – 18° of supercooling and produced single crystals by introducing a fine steel needle in the melt as a source of heterogeneous nucleation of the solid phase. The orientations of these single crystals, which were determined by x-ray diffraction method, were genetically related to the orientation of the primary nucleus of the solid phase. The stereographic projection of these crystallographic orientations is given in figure 3.1. Though their experiment gave a good picture of dendrite growth direction, the results are pretty scattered to come to a concrete conclusion.

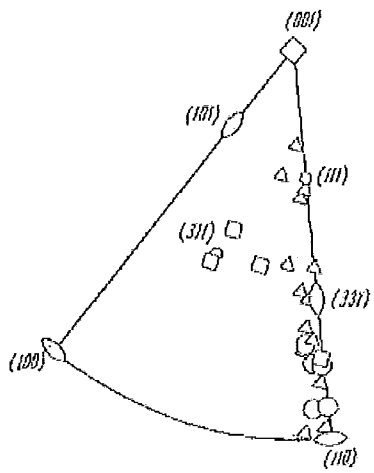

Figure 3. 1: Crystallographic orientation of the primary branches of dendrite developing along the free surface of the melt – triangle)$0<\Delta T<100$;circle) $10<\Delta T<120$; square)$12<\Delta T<180$ [121]

Nash and Glicksman [122] proposed a steady state dendrite growth model and following that model, Trivedi and Tiller [123] described interface morphology during crystallization taking Sn as an example. The Trivedi experiment proposed that the direction having the highest kinetic coefficient (μ_o) will be the dendrite growth direction and measured a specific value of the interface energy γ. But they did not consider the anisotropy in the interfacial free energy. Pokhorova [124] studied the time dependent growth of a dendrite with a nonisothermic surface considering an isotropic interfacial free energy.

The difficulty in experimental measurement and complex theoretical calculation has paved the way for computational modeling to be introduced in the study of interfacial energy and morphological development in dendrite forming systems.

3.2 Application of Atomistic Simulation in γ Computation

Over the years, two techniques have emerged as probable methods of computing crystal – melt interfacial energy, γ and its anisotropy from atomic scale MD simulations. One of the techniques is the cleaving technique, proposed by Broughton and Gilmer [125] which was later extended by Davidchack and Laird [126] and the other one is the capillary fluctuation method pioneered by Hoyt et al. [127]. A brief analysis of these two methods is given in the following sub – section.

3.2.1 Cleaving Technique

The cleaving technique directly calculates the solid–liquid interfacial free energy from MD simulations. This is a four step process that involves the reversible application and removal of an external potential in such a way that a crystal–liquid interface is formed from two separate bulk solid and liquid systems. The reversible work of the total process gives the interfacial energy γ. The anisotropy of $\gamma(\hat{n})$ can be mapped out by repeating the procedure for various crystal orientations. This method has been employed to compute γ for different model systems including hard spheres [128,129], soft spheres [130]

and LJ potential [131,132]. The initial formulation of the cleaving technique had a high extent of statistical uncertainties in its calculations to give a quantitative estimate of the anisotropy. Davidchack and Laird replaced the cleaving potentials with cleaving walls in this technique and obtained very accurate results for γ.

3.2.2 Capillary Fluctuation Method (CFM)

The Capillary Fluctuation Method (CFM) is based on MD measurements of the height of equilibrium fluctuations of the solid–liquid interface, from which the interface stiffness can be computed by employing capillary theory. In this research work, CFM will be followed to analyze the crystal – melt interface of pure Sn.

The CFM analysis begins with taking snapshots of crystal–liquid systems that have been equilibrated at the melting point using MD (pure materials) or MC (alloys). Periodic boundary conditions are employed in this method; that is, two solid–liquid interfaces are located within the simulation box. Snapshots of the simulation box give the position of the interfaces at a given time, which is located by a parameter defined as the order parameter, ϕ [117].

In real metallic systems, the crystal – melt interface is always a diffuse one. In CFM, the interface is located by labeling an atom as being either in the solid or liquid

phase by assigning an order parameter ϕ to each of the atoms in the system. The order parameter is defined as –

$$\phi = \frac{1}{n}\sum_i \left| \vec{r}_i - \vec{r}_{ideal} \right| \tag{3.3}$$

where $\vec{r}_{ideal}$ is the position of neighboring atoms in a ideal crystalline solid of a known orientation and $\vec{r}_i$ is the instantaneous position of atoms in the simulation box, n is the number of nearest neighbors and i is the nearest neighbor position over which the summation is taken. If the magnitude of the order parameter is low, that is the atom is nearly in the position of a crystalline state, then that atom is counted to be in the solid. Similarly, if the magnitude of the order parameter is high, that is the atoms are in random positions then it is taken to be in liquid state.

Snapshots of the interface are recorded in specific time intervals to monitor the height of a fluctuation. Fourier transformation of the height fluctuations produces the instantaneous value of the fluctuation amplitudes $A(k,t)$ which are averaged over all the simulated configurations to yield of the mean-square amplitude of capillary fluctuations given by $\left\langle \left| A(k_x, k_y \right|^2 \right\rangle$ where k_x and k_y are the wave vectors in two perpendicular directions parallel to the interface. For sufficiently large wavelength, the fluctuation spectra of a two dimensional fluctuating interface will follow the relation [128] –

$$\left\langle \left| A(k_x, k_y) \right|^2 \right\rangle = \frac{k_B T}{a(S_{xx}k_x^2 + S_{yy}k_y^2 + 2S_{xy}k_x k_y)} \tag{3.4}$$

where, S_{xx} and S_{yy} are the stiffness of the interface in direction perpendicular to the interface and a is the cross sectional area of the interface.

Crystalline symmetry can reduce the complexity of the computation. For the pure metal Sn, the (001) oriented interface has a four fold mirror plane symmetry that eliminates the S_{xy} term, and because $S_{xx} = S_{yy} = S$ for this condition, the equation 3.4 can be written in the following form –

$$\left\langle \left| A(k) \right|^2 \right\rangle = \frac{k_B T}{aS\ k^2} \tag{3.5}$$

The anisotropy components are included in the expansion of the stiffness term using spherical harmonics –

$$\gamma + \gamma'' = \gamma_0 (1 - \frac{\varepsilon_{20}\sqrt{5}}{\sqrt{\pi}} - \frac{27}{2}\frac{\varepsilon_{40}}{\sqrt{\pi}}) \tag{3.6}$$

The (110) oriented interface possesses a two fold symmetry and a mirror plane. This form of symmetry also eliminates the S_{xz} term but $S_{xx} \neq S_{yy}$. So the expression 3.4 reduces to the following form –

$$\left\langle \left| A(k_x, k_y) \right|^2 \right\rangle = \frac{k_B T}{a(S_{xx}k_x^2 + S_{yy}k_y^2)} \tag{3.7}$$

The angle dependent stiffness terms are expanded in the following way –

$$\gamma+\gamma''\big|_{xx}=\gamma_0(1-\frac{1}{4}\frac{\varepsilon_{20}\sqrt{5}}{\sqrt{\pi}}+\frac{9}{16}\frac{\varepsilon_{40}}{\sqrt{\pi}}+\frac{45}{16}\frac{\varepsilon_{44}\sqrt{35}\sqrt{2}}{\sqrt{\pi}}) \tag{3.8}$$

$$\gamma+\gamma''\big|_{yy}=\gamma_0(1+\frac{5}{4}\frac{\varepsilon_{20}\sqrt{5}}{\sqrt{\pi}}-\frac{171}{16}\frac{\varepsilon_{40}}{\sqrt{\pi}}+\frac{9}{16}\frac{\varepsilon_{44}\sqrt{35}\sqrt{2}}{\sqrt{\pi}}) \tag{3.9}$$

The (100) interface also possesses a two fold symmetry in Sn. The spherical harmonics expansion in terms of the anisotropic terms for this orientation is given in the following –

$$\gamma+\gamma''\big|_{xx}=\gamma_0(1-\frac{1}{4}\frac{\varepsilon_{20}\sqrt{5}}{\sqrt{\pi}}+\frac{9}{16}\frac{\varepsilon_{40}}{\sqrt{\pi}}-\frac{45}{16}\frac{\varepsilon_{44}\sqrt{35}\sqrt{2}}{\sqrt{\pi}}) \tag{3.10}$$

$$\gamma+\gamma''\big|_{yy}=\gamma_0(1+\frac{5}{4}\frac{\varepsilon_{20}\sqrt{5}}{\sqrt{\pi}}-\frac{171}{16}\frac{\varepsilon_{40}}{\sqrt{\pi}}-\frac{9}{16}\frac{\varepsilon_{44}\sqrt{35}\sqrt{2}}{\sqrt{\pi}}) \tag{3.11}$$

In different studies [129,130] of interfacial free energies it was found that for cubic materials, a three-term expansion is required to accurately capture the orientation dependence of the interface stiffness computed from MD.

3.3 Simulation Procedure for Pure Material: Sn

The CFM technique described in the previous section has been formulated for quasi 1-D fluctuating interface [117] which was later extended to a 2-D interface geometry [121]. In this research work, the 2-D formulation will be utilized to compute the independent stiffness values and extract the interfacial free energy and its associated anisotropies. In the 1-D computations, simulations have to be performed on three

orientations for complete analysis of the interface properties. Due to the body centered tetragonal structure of β Sn, in this study, simulations have been performed on (001), (100) and (110) interfaces.

Simulation technique in CFM requires an equilibrated interface in a crystal – melt system. Sn29 potential has been used here to generate a pure Sn system. Three simulation cells were used with the following dimension – for (001) orientation a 23×23×68 consisting 143888 atoms, for (100) orientation 66×24×24 consisting 152064 atoms and for (110) orientation $42\sqrt{2}\times21\sqrt{2}\times20$ consisting 136880 atoms. All the simulations have been conducted at the melting point as determined in section 2.4.2. The middle half of the simulation box was melted at a higher temperature to create a periodic boundary condition. After the melting step, the temperature of the whole simulation box is brought to the melting point in a NPAT ensemble with the cross sectional area normal to the direction chosen for computation kept fixed. The length in that direction was also allowed to change to relax the pressure and keep the system strain free.

After equilibrating, snapshots of the system were taken in a microcanonical (NVE) ensemble over a time period of 12 nano seconds in a time interval of 500 femto seconds. A total of 24000 configurations were collected for statistical analysis of the fluctuation spectrum given by $\left\langle \left| A(k_x, k_y) \right|^2 \right\rangle$.

3.4 Interfacial Stiffness Computation

The snapshots taken over the simulation period gave statistical information of the periodic solid – liquid Sn system. The first step of analyzing the data sets was to identify the crystal – melt interface that will give information about fluctuation spectra. The order parameter concept, as discussed in the section 3.2.2, was applied on the Sn system. For example, the simulation in (001) oriented interface, the simulation box and the associated order parameter profile is given in figure 3.2 (a) and (b) respectively. The computation was conducted over 10 nearest neighbor atom position. The deviation from their ideal position is computed over all the atoms at each corresponding z positions. It can be seen that at the two ends of the simulation box, the magnitude of the order parameter is low indicating the area to be in the crystalline state. This is to be expected as the atoms will be nearly in the ordered state. At the middle region, the order parameter jumps up suddenly as in the liquid region, the atoms will be in a random moving position. The interface is taken to be the region which will have an order parameter in the middle of the two extremes. Taking the interface order parameter too close to the lowest or highest point of the order parameter profile will result in errors in measuring the interface fluctuation. In the figure 3.2, the interface is taken to be in a position where order parameter ϕ has a magnitude of 1.25.

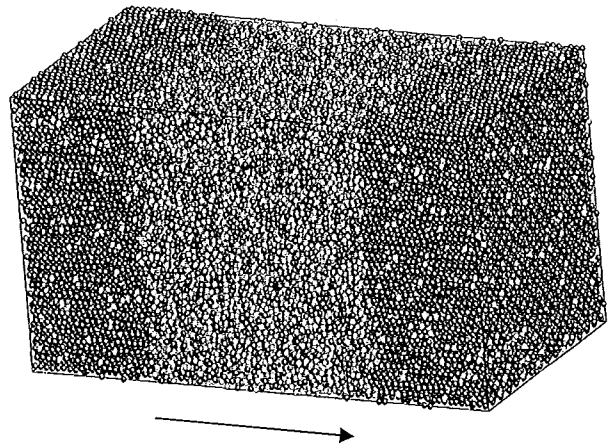

(a)

(b)

Figure 3. 2: Location of the crystal – melt interface in the Sn system set up with the Sn29potential (a) Simulation box with periodic boundary (b) Order parameter profile of the simulation box shown in figure (a)

The instantaneous fluctuation amplitudes are then measured from the height of the fluctuating interface and averaged over all the configurations to compute $\left\langle \left| A(k_x, k_y) \right|^2 \right\rangle$. The stiffness values are derived from the least square fit of a logarithmic plot of the fluctuation amplitude and the wave vector.

For the stiffness computation in the (001)[100] orientation, the expression in equation 3.3 was used. To fit the data, higher $|k|$ points were excluded due to the fact that at higher k points, the fluctuation amplitude might fall within the noise range in the system giving rise to uncertainties in its accuracy. Figure 3.3 shows the plot for $\left\langle \left| A(k) \right|^2 \right\rangle$ versus $|k|$ of this orientation.

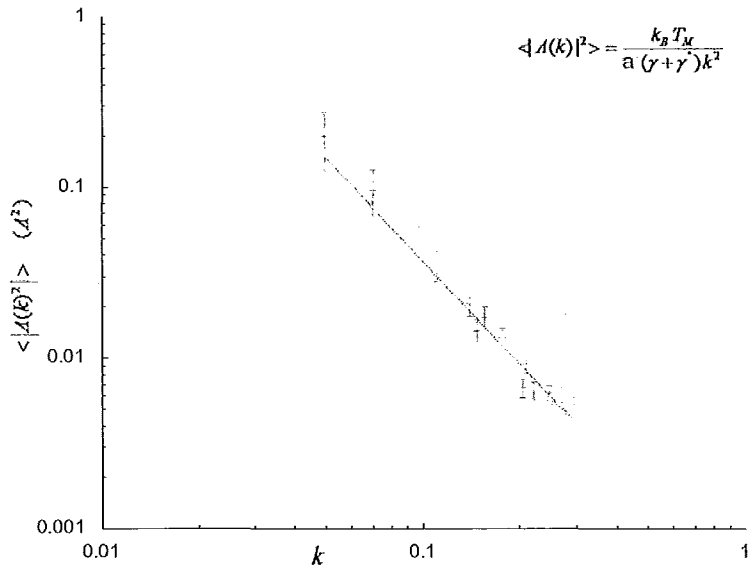

Figure 3. 3: $\left\langle \left| A(k) \right|^2 \right\rangle$ vs. $|k|$ plot for (001)[100] in the Sn29 simulated system

The slope of the amplitude – wave number plot includes the stiffness term as given in the equation 3.3. From the figure 3.3, the stiffness in the (001)[100] orientation was computed to be 126.41 ± 4.714 m J/m^2.

When the Sn29 system was used for analysis of the (100)[010] orientation, the crystal – melt interface showed almost no fluctuation on visual observation. Figure 3.4 shows the solid – liquid system with periodic boundary conditions and with the interface oriented at (100)[010]. CFM technique can not be applied on such an interface where there is no visible fluctuation of the interface.

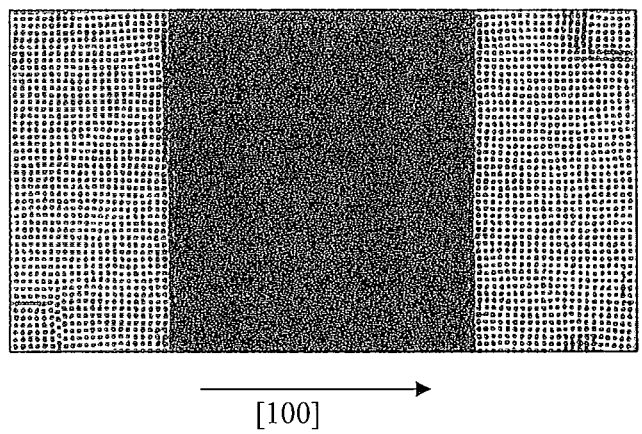

Figure 3. 4: A periodic solid – liquid system set up with Sn29 potential showing (100)[010] oriented crystal – melt interface as observed from the [001] direction.

When analyzing the data for (110)[001] and (110)[$1\bar{1}0$] it was found that (110)[$1\bar{1}0$] orientation was not following the general equation applicable for the CFM technique, as shown in equation 3.4, although (110)[001] showed good agreement.

The most plausible explanations of such a deviation can be given by the nature of interface in those specific orientations. CFM technique was originally formulated for atomically rough or diffuse interface; it can not explain the layer by layer growth of the flat or atomically smooth interface. The interface with (100)[010] and (110)[$1\bar{1}0$] orientations in Sn29 potential might posses such a flat interface which is causing it to deviate from the CFM general formula.

The atomically smooth interface shows up as a flat region in the equilibrium shape of a single crystal, which, in turn, is determined from Wulff plot of the crystal geometry. In the following section, a study on the Wulff plot of a single crystal of β Sn generated with Sn29 potential is described in detail.

3.5 Wulff Plot Construction and γ Computation

The equilibrium crystal shape is based upon the principle that a crystal will attain a shape that will minimize its surface free energy. In 1901, Wulff [133] proposed that the surface free energy of any body is an integral of the form –

$$\int \gamma(\hat{n}) ds \tag{3.5}$$

where the surface energy γ is, for anisotropic bodies, a function of the orientation of the unit outward normal $\hat{n}$ at each point of the surface S. If γ is plotted radially as a function of the direction $\hat{n}$, the plot will be sphere for an isotropic body and for systems with facetted interfaces, the surface energy plot will be like the outer surface in figure 3.5 (b).

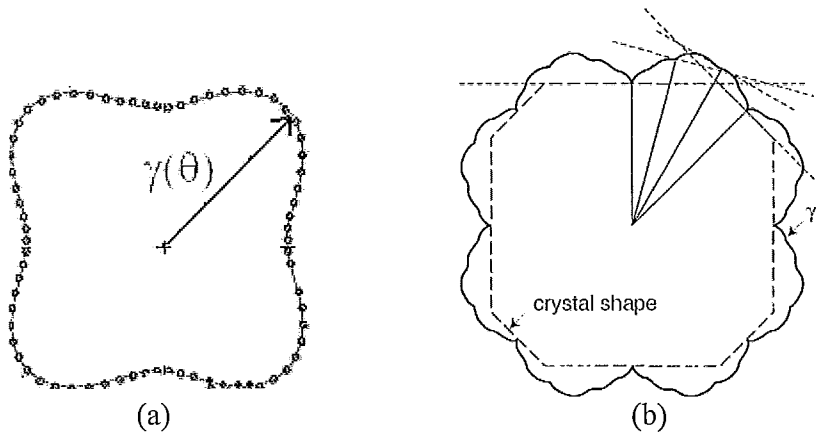

Figure 3. 5: Surface energy plot for (a) Materials with rough interface (b) Materials with facetted interface [153]

The deepest cusps in the 3.5(b) -plot are always present in the equilibrium when there are singular faces present in the system and the rounded regions are present where the interfaces are rough. If a group of vectors is drawn from a common origin whose length is proportional to the surface tension of the crystal face (the direction is perpendicular the face) and at the end of each vector a plane perpendicular to the vector direction is constructed, then the shape enclosed by the planes gives the equilibrium shape of the crystal. In the figure 3.5 (b), the dotted line gives the equilibrium shape of

the crystal with a surface energy plot given by the outer lines. Experimentally, the equilibrium shape can be determined by annealing small single crystals at high temperatures in an inert atmosphere or conducting similar experiments on small voids inside a crystal [119].

In this study, a simulated experiment was conducted to determine the equilibrium shape of a single crystal of Sn with Sn29 potential. A β Sn system with a dimension of 64 ×64×8 unit cells, consisting of 131072 atoms, was generated using the Sn29 potential. A region with 47.68 Å diameters (8 unit cells) was selected in the middle of the system. A curvature corrected melting point of that region was estimated to be 531K instead of 547K for Sn29 potential. The whole system was equilibrated in an NP_xAT ensemble at 531K temperature. Keeping that region in the crystalline state, the surrounding region was melted at a higher temperature. The whole system was again equilibrated at 531 K making a single disk shape crystal to be in equilibrium with its melt at the melting point. The whole equilibrated system looked like figure 3.6 .

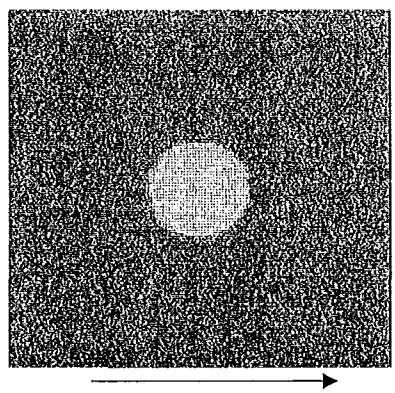

Figure 3. 6: The equilibrated crystal – melt system of β Sn with Sn29 potential

A microcanonical ensemble (NVE) was applied to this system at the curvature corrected melting point for 4 nano seconds and snapshots of the entire system was collected after every 50 pico seconds. The system looked like figure 3.7 after the 4 nano seconds run.

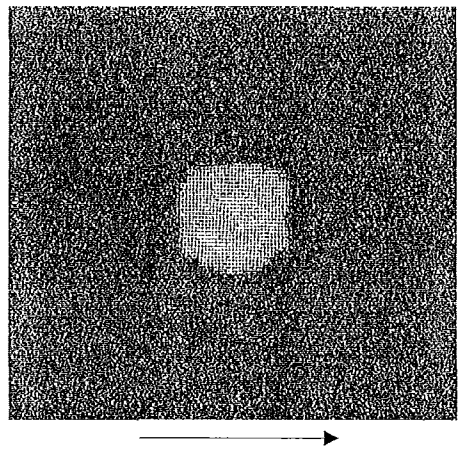

Figure 3. 7: The crystal – melt system after equilibration at 531 K after 4 nano seconds.

In figure 3.8, the positions of atoms with low order parameter have been plotted over many snapshots. The flat interfaces at (100)[010] and (110)[$1\bar{1}0$] orientations is clearly visible in the figure. The disk shape single crystal did not change its position in the crystal – melt system by the application of any buoyancy force from the liquid. This fact is evident from the density profile of atoms as shown in figure 3.9. The profile shows the density of atoms with low magnitude of order parameter; that is the density profile of atoms in the solid. The profile has peak at the middle of the system, indicating that the disk shape single crystal stayed stationary at the centre of the crystal – melt system.

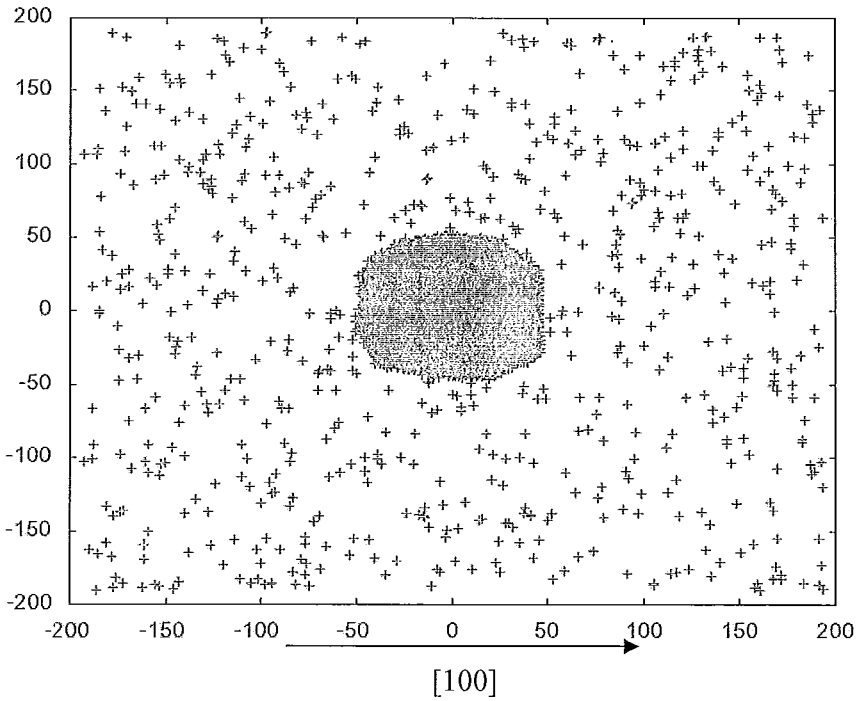

Figure 3. 8: The position of atoms having low magnitude of order parameter in the entire system.

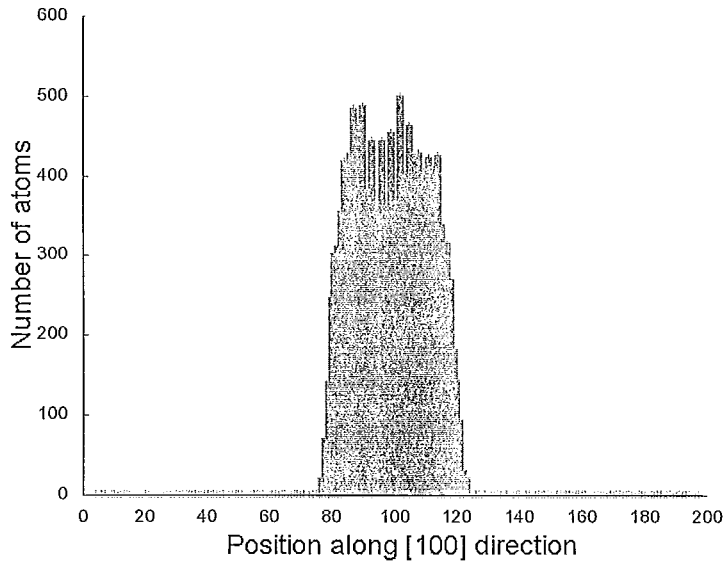

Figure 3. 9: Density profile of solid atoms in the crystal – melt system set up with Sn29

An approximate estimation of the interfacial energy γ_{100} and γ_{110} was computed by measuring the length of the sides of the equilibrium shape of the single crystal as shown in figure 3.8. The details of the calculation is given in appendix A. The estimated value of γ_{100} was found to be 14.70 mJ/m^2 and γ_{110} was found to be 20 mJ/m^2. By comparison with literature values, all the published result of interfacial energy for crystal – melt interface in Sn was measured without the anisotropic affect taking into consideration. The anisotropic solid – liquid interfacial energy measured by Trunbull [112] was 54.5 mJ/m^2 and the result published by Trivedi [123] gives a value of 36 mJ/m^2.

CHAPTER 4

Computation of Kinetic Coefficient of Crystal – Melt Interface

4.1 Interface kinetics and growth morphology

The mobility of a molecularly rough solid – liquid interface is given by the kinetic coefficient μ. The kinetic coefficient is defined as the proportionality constant between growth velocity and the undercooling at the crystal – melt interface. If the undercooling at the interface is given by $\Delta T = T_M(P) - T$, where $T_M(P)$ is the melting point at zero pressure, the interface velocity is related to the undercooling by the following relation –

$$V = \mu \Delta T \qquad (4.1)$$

μ is the kinetic coefficient in the equation 4.1. For most dendrite forming metallic systems at high velocities, the magnitude and crystalline anisotropy associated with μ are very critical factors which govern the growth rate and morphological development is cast structures [134 – 136].

Because of the inherent difficulties, very few studies have been conducted on experimental determination of the kinetic coefficient and interface mobility in solidification of a crystal from its melt [137,138] In the more recent works to improve the

theoretical understanding of this concept and to develop mathematical models, computational modeling, more specifically atomic scale molecular dynamics (MD) and Monte Carlo simulations are being used most effectively. One of the pioneering MD studies was conducted by Broughton, Gilmer and Jackson [139] on crystal growth simulation of a Lennard – Jones (LJ) system. Their model described the LJ system by a collision limited growth, where the interface motion depends upon the frequency of collisions of the liquid atoms on the crystal interface. Though this model contradicted the earlier theories of crystallization kinetics, defined by the diffusion governed thermal activation model of Wilson and Frenkel [140, 141], it produced good agreement with the results published by Turnbull and co-workers [142,143]. The main drawback of this model was it did not include the underlying crystalline anisotropy; rather it was governed by the differences in *d* spacing.of the crystalline planes normal to the growth direction. In 1988, Burke et al. [144] investigated further the crystallization kinetics of LJ systems by MD, and found that interfaces in some specific orientations were moving faster than other orientations of the system. Bragard et al. [145] demonstrated that this difference in kinetics at different orientation plays an important role in the selection of growth morphology and dendrite tip velocity at high undercooling. Though several models have been proposed so far for the kinetic anisotropy for molecularly rough interfaces, a clear understanding in this regard has not been achieved yet.

Very few experimental works have been conducted so far to determine the crystallization kinetics of the pure element Sn. Yesin et al. [140] conducted experiments on

Sn at different undercooling to understand the relation between growth rates and driving force but their result had considerable amount of scatter to come to a concrete conclusion. Trivedi and Tiller [123] proposed a model for determining interface morphology during crystallization and computed the kinetic coefficient for Sn. Dvinyaninov and Romanenko [146] developed another model for determination of the kinetic coefficient of crystallization, matched their model with the experimental results for Sn conducted by Kramer and Tiller [147] and found good agreement. But none of the research conducted so far on Sn considered the underlying crystalline anisotropys.

In this study, Molecular Dynamics have been used to model crystal – melt interface of Sn and the kinetic coefficient has been computed for specific orientations. The details of the computation are described in the following sections.

4.2 MD study of Sn crystal growth

Several methods have been developed so far to compute the kinetic coefficient using Molecular Dynamics. These methods can be categorized into different classes – forced velocity simulations, free solidification, imposed pressure simulations and fluctuation analysis method. In this research work, *Free Solidification Method* and *Capillary Fluctuation Method* have been employed to determine the kinetic coefficient of the crystal – melt interface of Sn. The Sn29 potential described in Chapter 2 has been used in this study to generate the Sn system. In the previous chapter, it was found that in

Sn29 potential, the (110)[001] and (110)[$1\bar{1}0$] orientation of the crystal – melt interface is flat or atomically smooth. The kinetic coefficient, by definition, can be computed for atomically rough or diffuse interface. Due to this restriction, the kinetic coefficient only in the (001)[100] orientation is computed in this study. A detailed description of the computation process is given in the following sub – sections.

4.2.1 Free Solidification Method

The Free Solidification (FS) method is a non – equilibrium MD (NEMD) approach to compute the interface kinetics. This method has been applied by a number of authors in previous occasions [148 – 151]. It involves a solid – liquid system with a periodic crystal melt interface, equilibrated at the melting point. Application of a constant temperature field below the melting point acts as the driving force for solidification. The interface movement during the solidifying process is monitored through the track of the potential energy change which leads to the determination of the growth velocity V as a function of undercooling, ΔT.

The solid – liquid system in this method is characterized by two constraints given by the constant number of atoms in the whole system and the total potential energy of the system is a weighted sum of the potential energy of the solid and the liquid phase. The first condition ensures that $N_T = N_S + N_L$ where N_T, N_S and N_L are the number of atoms in the entire system, in the solid and in the liquid respectively. The second condition states

that $N_T E_T = N_S E_S + N_L E_L$ where E_T, E_S, E_L are the potential energy of the system, solid and liquid respectively. Solving the equations for these two constraint, the expression for the temperature dependent growth velocity can be given by the following expression –

$$V(\Delta T) = \frac{\dot{E} N_T V_S}{2a(E_L - E_S)} \tag{4.2}$$

where, $\dot{E}$ is the slope of the potential energy per atom versus time plot, N_T is the total number of atoms in the system, V_S is the volume per atom of the bulk solid phase at the melting point, a is the cross sectional area of the simulation cell and E_L and E_S are the potential energy per atom of the bulk solid and liquid phase at the melting point. The *2* in the equation is due to the periodic boundary condition; there are two solid – liquid interfaces in the system. The kinetic coefficient μ is then computed from the equation 4.1.

To compute the kinetic coefficient of Sn, a 12 × 12 × 42 system consisting 24192 atoms was generated using the Sn29 potential. The solid – liquid system was created by melting the middle half of the system along the *z* direction at higher temperature. The whole system was then equilibrated in a NP_ZAT ensemble at the melting point of 547K. The pressure and temperature was monitored to achieve a steady state and to make sure that the system is free from any other from of external driving force. After the equilibration stage, an undercooling of 60K was applied over a time span of 10 nano seconds on the entire system to initiate the movement of the crystal – melt interface. In figure 4.1, the snapshots taken at every 2 ns show the interface moving towards each other and after the 8^{th} nano second, the entire system was found to have solidified.

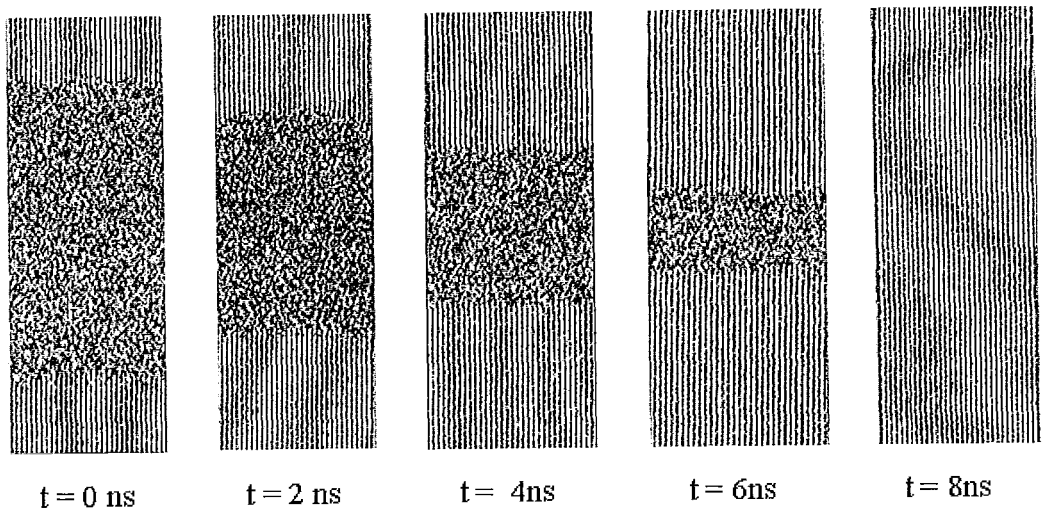

Figure 4. 1: Snapshots of the solid – liquid system after the application of the 60K undercooling at 2 ns time interval

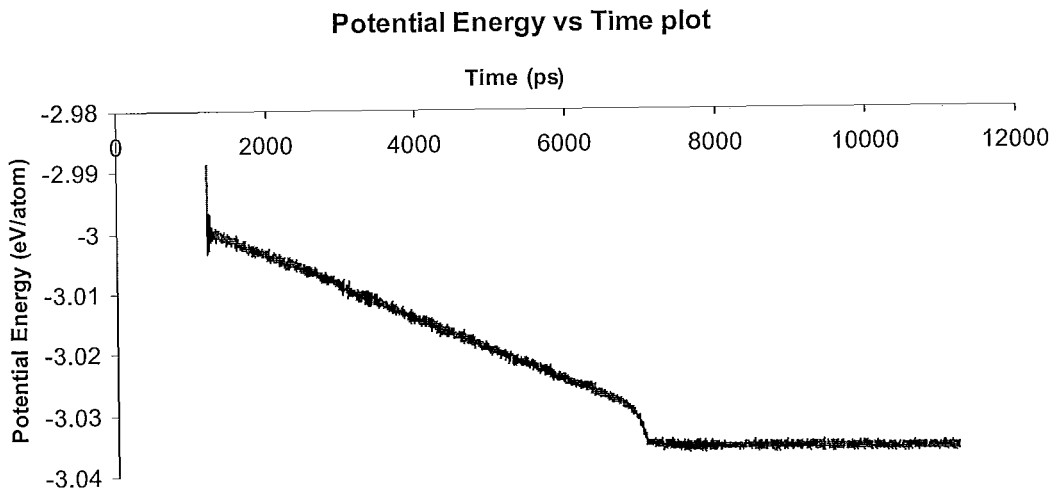

Figure 4. 2: Potential energy per atom as a function of time during the solidification of the (001)[100] interface at 60K undercooling.

The figure 4.2 denotes the change in potential energy per atom during the solidification process due to the application of the 60K undercooling. From that plot, $\dot{E}$ is measured, and substituting the values in equation 4.2, the magnitude of kinetic coefficient in the (001)[100] orientation was found to be 1.4 ± 0.1 cm/s/K.

4.2.2 Capillary Fluctuation Method (CFM)

The kinetic coefficient can be extracted from the dynamics of the fluctuation of the crystal – melt interface. Fluctuation methods can be applied on a system in equilibrium, and thus provide an independent check of values derived from the non-equilibrium MD methods described in the previous sub – section. In this technique, the time dependent fluctuation amplitude is measured to compute the kinetic coefficient. The sinusoidal fluctuation amplitude at the atomic scale shows an exponential decay with time, which is governed by the following kinetic equation [148] –

$$\langle A(k,t)A^*(k,0)\rangle = \langle |A(k)|^2 \rangle \exp(-\frac{t}{\tau}) \qquad (4.3)$$

where $A(k,t)$ is the Fourier transform of the interface height, $A^*(k,0)$ is the reference amplitude evaluated at some arbitrary time. The τ in the equation is the relaxation time which is given by –

$$\tau = (\Gamma \mu k^2)^{-1} \qquad (4.4)$$

The Γ in the equation 4.4 is the capillary length, defined as $\Gamma = (\gamma + \gamma'')\frac{T_M}{L}$. The term $(\gamma + \gamma'')$ is the interfacial stiffness, which is described in detail in chapter 3, T_M is the

melting point and L is the latent heat per unit volume. The relaxation time τ is calculated for each value of k by fitting the exponential decay of the autocorrelation function $\langle A(k,t)A^*(k,0)\rangle$ in the equation 4.3. The Fourier amplitude of the fluctuating interface is related to the interfacial stiffness by the capillary theory [127]. The kinetic coefficient, in turn, can be extracted from the slope of the Fourier amplitude with relaxation time plot, which can be expressed by the following relation –

$$\langle |A(k)|^2 \rangle = \left[\mu \frac{k_B T_M^2}{aL} \right] \tau \tag{4.5}$$

where, a is the cross sectional area of the simulation cell.

In this study, the *CFM* technique for computing the kinetic coefficient was applied on the system that was used to determine the interface stiffness in the (001)[100] oriented interface. The detailed description of the system is given in section 3.3. The relaxation time τ for each k point was determined from exponential fits of the fluctuation data collected over the 12 nano seconds run at a time interval of 500 femto seconds. In the figure 4.3, the decay of the autocorrelation function $\langle A(k,t)A^*(k,0)\rangle$ versus the reduced time $\frac{t}{\tau}$ is shown for one k point.

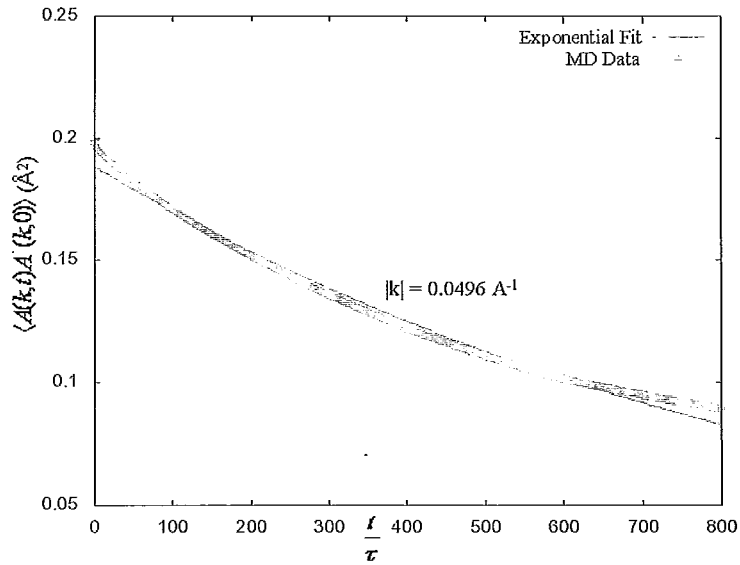

Figure 4. 3: $\langle A(k,t)A^{*}(k,0)\rangle$ vs the reduced time $\frac{t}{\tau}$ for Sn29 potential system. The data from the kinetic fluctuation technique are shown by the green line and the best fit to the exponential decay is given by the red line.

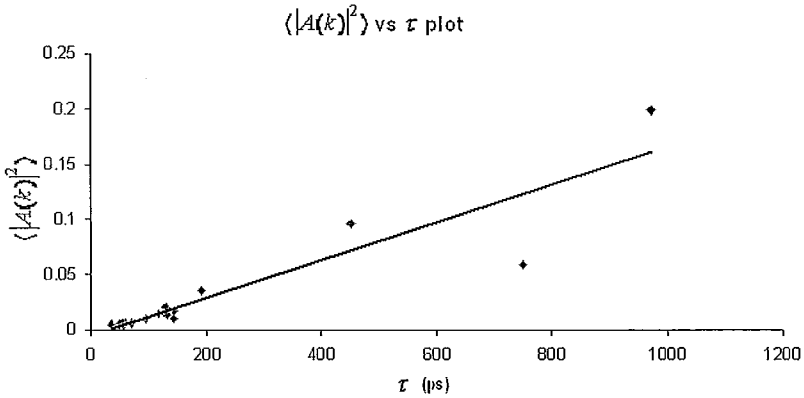

Figure 4. 4: $\langle |A(k)|^{2}\rangle$ vs relaxation time τ for a Sn29 system. The crystal – melt interfaces oriented at (001)[100] direction.

From the plot of $\langle |A(k)|^2 \rangle$ vs τ, as shown in figure 4.4, the kinetic coefficient is extracted from the slope of that curve. The kinetic coefficient in the (001)[100] orientation as computed from this experiment was 1.75 ± 0.09 cm/s/K

Comparing the results, it was found that the kinetic coefficient for the (001) [100] orientation was very close to each other for the two methods. When compared with the results found in literature, as can be seen from table 4.1, there is a wide variation in the data in the published experiments. This can be attributed to the fact that none of the experiments considered the anisotropy effect in computing the kinetic coefficient.

Table 4. 1: Comparison of results as found in literature with the result of this study

Results	Kinetic coefficient
Yesin et al. [152]	11.62 cm/s/K
Trivedi and Tiller [123]	4.0 cm/s/K
Computed from this research	μ_{001} = 1.43 ± 0.124 cm/s/K (Free solidification method)
	μ_{001} = 1.746 ± 0.089 cm/s/K (Capillary Fluctuation method)

CHAPTER 5

Conclusion

In this research work, a computational model for Sn has been developed and its solid – liquid interface properties have been computed utilizing Molecular Dynamics atomistic simulation technique. The conclusions that can be drawn from this work are described in the following –

1. The modified embedded atom method is a classical interatomic potential scheme capable of simulating systems exhibiting both metallic and covalent bonding. Using this method, a previously published pure Sn potential, by Ravelo and Baskes [86], has been evaluated to asses its universal applicability as a computational model of Sn. The RB potential was found to posses some weaknesses which prevents its use in setting up equilibrium crystal – melt system of Sn.

2. The RB potential has been modified to overcome the complications in its computation of melting properties. A new set of potential parameters were developed, which is referred to as Sn29 potential. The Sn29 potential was

evaluated in the same way as RB potential was evaluated, and it was found to be free from the weaknesses of the RB potential.

3. Structural properties have been computed with the new Sn29 potential. Good agreement was found with the results in published literature. The main deviation occurred in the c/a ratio of the β phase, but this parameter is still within 1% of the experimental value.

4. Thermodynamic properties computed from Sn29 agree well with experiments. It predicts the correct stability of phases at different temperatures and also improves upon the melting properties. The latent heat of melting and heat of phase transition is comparable with those of other experimental results.

5. The main weakness of Sn29 potential was found in its computation of elastic properties. The values of the elastic constants vary from the results computed by the RB potential and also from the experimental results published in literature. But the bulk modulus agrees well with literature.

6. The crystal – melt interfacial stiffness in the (001)[100] orientation have been computed from Molecular Dynamics simulation utilizing the Capillary Fluctuation Method (CFM).

7. No fluctuation of the interface was observed on the (100)[010] and (110)[$1\bar{1}0$] orientation of the crystal – melt interface, set up with the Sn29 potential.
8. Wulff plot was constructed for a single crystal set up with Sn29 potential. The interface in the (100)[010] and (110)[$1\bar{1}0$] orientation showed up as flat or atomically smooth interface the in the plot.

9. An approximate measurement of the interfacial energy was done from the Wulff plot and γ_{100} was found to be 14.70 mJ/m^2 and γ_{110} was found to be 20 mJ/m^2.

10. The kinetic coefficient in the (001)[100] orientation was computed utilizing Capillary Fluctuation Method (CFM) and Free Solidification Method (FSM). The results were found to be μ_{001} = 1.43 ± 0.124 cm/s/K for FSM and μ_{001} = 1.746 ± 0.089 cm/s/K.for CFM.

CHAPTER 6

Future Work

From the experiments and analysis conducted in the research work, some scope of further study came up which are suggested in the following –

1. The RB potential was modified to produce Sn29 for better melting properties of pure Sn. Further research is required to improve upon the elastic properties of the Sn29 potential to develop an optimum computational model for Sn.

2. The (100)[010] and (110)[$1\bar{1}0$] orientation in Sn29 potential was found to be flat or atomically smooth. A better understanding of the atomic scale interaction taking place at the crystal – melt interface in those orientations is required to understand the growth morphology of Sn crystal.

3. Addition of alloying elements will have an effect upon the interface properties of pure Sn. Further research is required to understand this effect as most of the major applications of Sn is in the form of Sn alloys.

APPENDIX A

Calculation of γ_{100} and γ_{110}

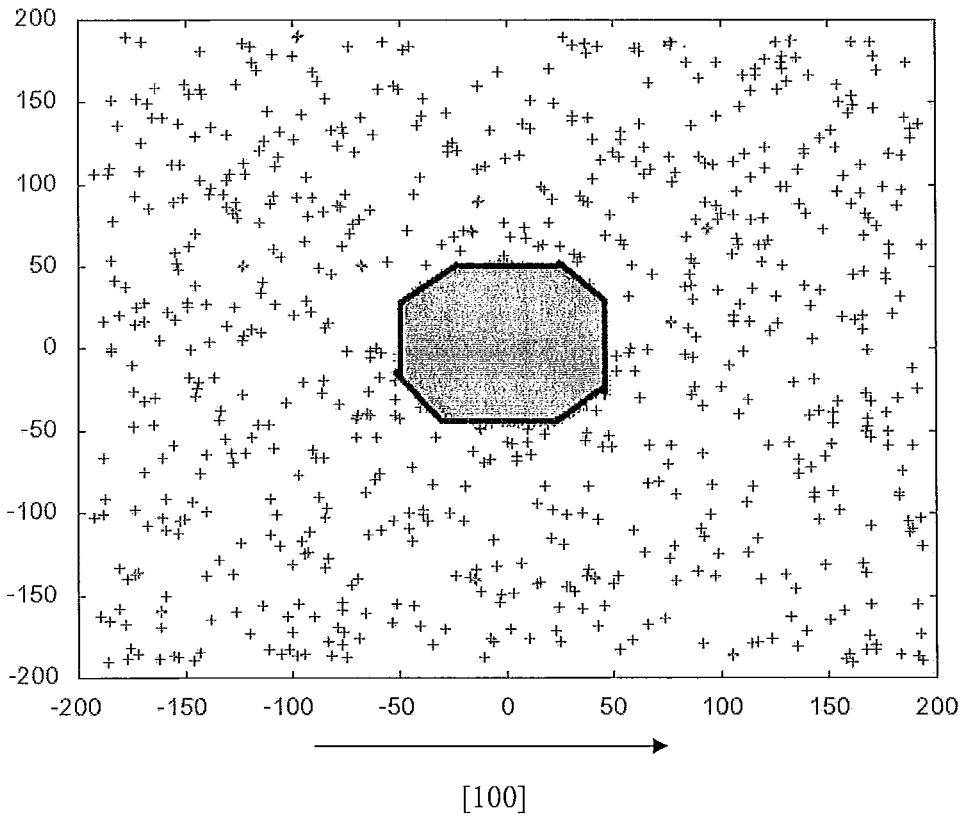

Figure A1: The crystal – melt system as described in section 3.5

The system, as described in section 3.5, is shown in figure A1 with the crystal – melt interface outlined to show the change in shape of the single crystal disk on which the

experiment was conducted. In figure A2, a schematic diagram of the crystalline solid in the system and its approximate measurement is shown.

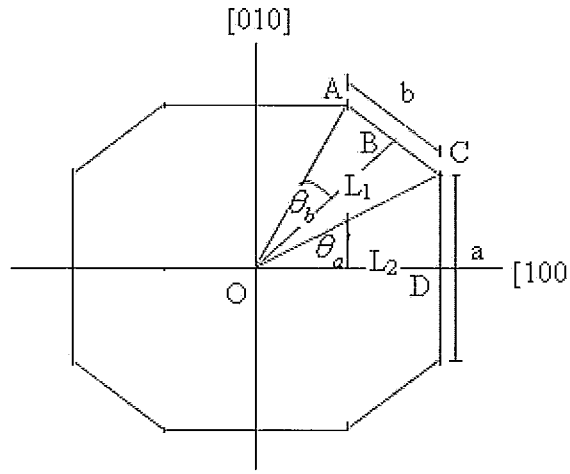

Figure A2: Schematic diagram of the crystalline solid in figure A1.

Applying Wulff theory on the schematic diagram in A2, the following relation can be described –

$$\frac{\gamma_{100}}{L_1} = \frac{\gamma_{110}}{L_2}$$

$$\Rightarrow L_1\gamma_{110} = \alpha L_1\gamma_{100} \qquad \text{(A1)}$$

where, $L_2 = \alpha L_1$

The free energy change in the system due to solidification on the surface of the disc shape crystal given by –

$$\Delta G = -V_s\Delta G_V + A_{SL}\gamma_{SL} \qquad \text{(A2)}$$

If the thickness of the disc is t then –

total volume of the octagon, $V_s = 2aL_1t + 2b\alpha L_1t$ (A3)

total surface area of the crystal – melt interface, $A_{SL} = 4at + 4bt$ (A4)

From figure A2, $\angle BOC + \angle\theta_a = 45°$ and $\angle BOC = \angle\theta_b$

So, $\angle\theta_a + \angle\theta_b = 45°$

From ΔAOB and ΔCOD, the following relations can be derived –

For, ΔAOB

$$\frac{a}{2} = L_1 \tan\theta_a$$

$$\Rightarrow a = 2L_1 \tan\theta_a$$

For, ΔCOD

$$\frac{b}{2} = L_2 \tan\theta_b$$

$$b = 2\alpha L_1 \tan(45 - \theta_a)$$

$$b = 2\alpha L_1 \frac{1 - \tan\theta_a}{1 + \tan\theta_a} \quad \text{(A5)}$$

So, equation A3 and A4 can be written in the following form –

Volume of Octagon, $V_s = \left(4L_1^2 \tan\theta_a + 4\alpha^2 L_1^2 \frac{1 - \tan\theta_a}{1 + \tan\theta_a}\right)t$ (A6)

Surface area of the crystal – melt interface, $A_{SL} = \left(8L_1 \tan\theta_a + 8\alpha L_1 \frac{1 - \tan\theta_a}{1 + \tan\theta_a}\right)t$ (A7)

The equation A5 and A6 can be substituted in A1 –

$$\Delta G = \left(-4L_1^2 \tan\theta_a - 4\alpha^2 L_1^2 \frac{1 - \tan\theta_a}{1 + \tan\theta_a}\right)t\Delta G_v + \left(8L_1\gamma_{100} \tan\theta_a + 8\alpha L_1\gamma_{110} \frac{1 - \tan\theta_a}{1 + \tan\theta_a}\right)t$$

Taking derivative of this equation with respect to L_1 and setting it to 0, the following relation is obtained –

$$\left(-L_1 \tan\theta_a - \alpha^2 L_1 \frac{1 - \tan\theta_a}{1 + \tan\theta_a}\right)\Delta G_v + \left(\gamma_{100} \tan\theta_a + \alpha\gamma_{110} \frac{1 - \tan\theta_a}{1 + \tan\theta_a}\right) = 0 \quad \text{(A8)}$$

In the equation A6, the term ΔG can be written as $\Delta G = \frac{L_V \Delta T}{T_m}$.

For Sn29, L_V is 0.00162 ev/ Å^3 and in this experiment ΔT is 16K and T_m is 547K giving a value of 4.74×10^{-5} ev/ Å^3 for ΔG in this experiment.

Approximate measurement of the components in the figure A1 gives the following –

$L_1 = 19.24$ Å,

$a = 22.22$ Å

$b = 14.11$ Å

$\theta_a = 30^0$

Introducing these values in the expression A5, it is found that $\alpha = 1.36$.

So, the expression A8 becomes

$$0.57\gamma_{100} + 0.36\gamma_{110} = 9.78\times10^{-4} \qquad \text{(A9)}$$

Solving equation A1 and A9, it is found that –

$\gamma_{100} = 20$ mJ/m^2

$\gamma_{110} = 14.70$ mJ/m^2

References:

1. http://www.itri.co.uk/pooled/articles/BF_TECHART/view.asp?Q=BF_TECHART_30_9008
2. Hampshire W B & Killmeyer A J, *Journal of metals* **41** 32 (1989)
3. Oladele A. Ogunseitan, *Journal of Materials*, **59**, 12 (2007)
4. Melton C, *Surface Mount Technology*, **9**, 6 (1995)
5. Hirano, T, Fukuda, K, Ito, K, Kiga, T & Taniguchi, Y, *Proceedings of the 2001 IEEE International Symposium on Electronics and the Environment* (2001)
6. Castello, T, Rooney, D & Dongkai S, *Soldering & Surface Mount Technology*, **18** 21 (2006)
7. Abdulhamid, F, Li, S & Basaran, C, *International Journal of Materials and Structural Integrity*, **2**,11 (2008)
8. Hongjin J & Wong, C P, *IEEE Nanotechnology Magazine*, **4**, 20 (2010)
9. Park, M S & Arróyave, R, *Acta Materialia*, **58**, 4900 (2010)
10. National Center for Manufacturing Sciences, *Lead-Free Solder Project Final Report*, NCMS ProjectNo. 170502.
11. Edwin Bradley et al, *Lead-free electronics: iNEMI projects lead to successful manufacturing,* IEEE Press/Wiley-Interscience, Piscataway, NJ, 2007
12. Evans C J *Tin and Its Uses* **142** 13 (1984)
13. Mining and Quarry World, **3**, 8 (2006)
14. Paul W *J. Appl. Phys.* **32** 2082 (1961)

15. Cohen, O L & Van Leishout, A K W A, *Z. Phys. Chem. A* **173,** 32 (1935)

16. Tin Research Institute, *The Properties of Tin*, Publication 218 (1954)

17. Ojima, K, Taneda, A & Takasaki, A, *Phys. Stat. Sol. A* **139**, 139(1993)

18. Walther, J H & Koumoutsakos, P, *Journal of Heat Transfer*, **123**, 741 (2001)

19. Komanduri, R., Chandrasekaran, N. & Raff, L.M, *International Journal of Mechanical Sciences*, **43**, 2237 (2001)

20. Itoh, S.& Igami, M, *Proceedings of the International Conference of Computational Methods in Sciences and Engineering 2003 (ICCMSE 2003),* 250 (2003)

21. Suits, F, Pitman, M C, Pitera, J W, Swope, W C & Germain, R S, *IBM Journal of Research and Development*, **49**, 475 (2005)

22. Egami, T., *Journal of Materials*, **62**, 70 (2010)

23. Hill, T L, *An introduction to statistical thermodynamics*, Dover Publication, NY (1987)

24. Qia, W H., Wanga, M.P. & Hub, WY., *Materials Letters*, **58,**1745 (2004)

25. Zientarski, T & Chocyk, D., *Molecular Physics*, **105**, 3099 (2007)

26. Moosavi M & Goharshadi, E K, *Fluid Phase Equilibria*, **274,** 51 (2008)

27. http://employees.csbsju.edu/hjakubowski/classes/ch331/protstructure/ilennardjones2.gif

28. Halicioglua, T and Cooper, D M, *Materials Science and Engineering*, **62**, 121 (1984)

29. Shi, L T, *Materials Science and Engineering*, **81**, 509 (1986)

30. Laricchiuta, A., Colonna, G., Bruno, D., Celiberto, R., Gorse, C., Pirani, F. and Capitelli, M., *Chemical Physics Letters*, **445**, 133 (2007)

31. Xu, Y., Xu, D. and Liang, J., *Computational Methods for Protein Structure Prediction and Modeling*, Springer, NY (2007)

32. Daw, M.S., Baskes, M. I., *Physical Review B*, **29**, 6443 (1984)

33. Daw, M.S., Foiles, S.M. and Baskes, M.I., *Material Science Reports*, **9**, 251 (1993)

34. Parr, R. G. & Yang, W., *Density-Functional Theory of Atoms and Molecules,* Oxford University Press, US (1994)

35. Adams, J. & Foiles, S., *Physical Review B*, **41**, 3316 (1990)

36. Johnson, R.A. and Oh, D.J., *Journal of Materials Research,* **4**, 1195 (1989)

37. Finnis, M W, and Sinclair, J E, *Philosophical Magazine A*, **50**, 45 (1984)

38. Rosato, V.,Guillope, M., and Legran, B., *Philosophical Magazine A*, **59**, 321 (1989)

39. Sutton, A. P. and Chen, J., *Philosophical Magazine Letters*, **61**, 139 (1990)

40. Baskes M. I., *Physical Review B (Condensed Matter)* **46**, 2727 (1992)

41. Ramalingam H, Asta M, Van de Walle A and Hoyt J J, *Interface Science*, **10** 149 (2002)

42. Rose J H, Smith J R and Ferrante G F, *Physical Review B* **29** 2963 (1984)

43. Flemings, M. C., *Metallurgical and Materials Transactions B,* **5**, 2121 (1974)

44. Davidge, R.W., *Symposium on Fracture Mechanics of Ceramics. Vol.II*, (1974)

45. Hajnal, M, Konyves-Toth, M. & Reti, T., *Proceedings of the 9th IMEKO Congress of the International Measurement Confederation*, (1982)

46. Askeland, D. R., *The science and engineering of materials*, PWS Publishers, USA (1984)

47. Kim S.W., Lee U.J., Woo K.D. & Kim D.K., *Materials Science and Technology*, **19,** 1727 (2003)

48. Li, J. C., *Microstructure and Properties of Materials*, World Scientific, Singapore (2000)

49. Dutta, A. K., Narasaiah, N., Chattopadhyay, A. B. & Ray, K. K., *Materials and Manufacturing Processes*, **17**, 651 (2002)

50. Furrer, D U & Semiatin, S L, *Metalworking: Bulk Forming,* **14A**, 374 (2005)

51. McCormick, M. & Jin, S., *Electronics Manufacturing Technology Symposium*, **1**, 14 (1994)

52. Shangguan, D., *Lead-free solder interconnect reliability*, ASM International (2005)

53. Kang, S. K., Lauro, P. A, Shih, D.Y., Henderson, D. W. and Puttlitz, K. J, *IBM Journal of Research and Development*, **49**, 607 (2005)

54. Glazer, J., *Journal of Electronic Materials*, **23**, 693 (2007)

55. Nguyen, J., Geiger, D., Rooney, D. & Shangguan, D., *Electronics Packaging Manufacturing*, **31**, 239 (2008)

56. http://www.umms.sav.sk/index.php?ID=1713

57. Müller-Krumbhaar, H. and Langer, J. S., *Acta Metallurgica*, **26**, 1681 (1978)

58. Trivedi, R., *Journal of Crystal Growth*, **49**, 219 (1980)

59. Glicksman, M. E. , *Materials Science and Engineering*, **65**, 45 (1983)

60. Amar, M. B., Pomeau, Y., *Europhys. Lett*, **2** 307 (1986)

61. Furukawa, Y. & Shimada, W., *Journal of Crystal Growth*, **128**, 234 (1993)

62. Stupian, G.W. & Presser, N., *Aerospace Applications Conference*, 397 (1994)

63. Ivantsov, G. P., *Dow. Akad. Nauk SSSR*, **58**, 567 (1947)

64. Saito, Y., Goldbeck – Wood, G. & Muller – Krumbhaar, H., *Physical Review A*, **38**, 2148 (1988)

65. Karma, A. & Rappel, W. J., *Physical Review Letter*, **77**, 4050 (1996)

66. Karma, A. & Rappel, W. J., *Physical Review E*, **57**, 4323 (1998)

67. Plapp, M. & Karma, A., *Physical Review Letter*, **84**, 1740 (2000)

68. Plapp, M. & Karma, A., *Journal of Computational Physics*, **165**, 592 (2000)

69. Provatas, N., Goldenfield, N. & Dantzig, J., *Physical Review Letter*, **80**, 3308 (1998)

70. Bragard, J., Karma, A., Lee, Y. H. & Plapp, M., *Interface Science*, **10**, 121 (2002)

71. Chen, L. Q., *Annual Review of Materials Research*, **32**, 113 (2002)

72. Hoyt, J. J., Asta, M. & Karma, A., *Materials Science and Engineering R*, **41**, 121(2003)

73. Glicksman, M. E. & Singh, N. B., *Journal of Crystal Growth*, **98**, 277 (1989)

74. Liu, X.Y., Boek, E.S., Briels, W.J. & Bennema, P., *Nature*, **374**, 342 (1995)

75. Rappaz, M., Friedli, J., Mariaux, A. & Salgado-Ordorica, M., *Scripta Materialia*, **62**, 904 (2010)

76. Morris, J. R. & Napolitano, R. E., *Journal of the Minerals, Metals and Materials Society*, **56,** 40 (2004)

77. Glicksman, M.E. & Singh, N.B., *Journal of Crystal Growth*, **98** 277 (1989).

78. Muschol, M., Liu, D., & Cummins, H., *Physical Review A*, **46** 1038 (1992)

79. Hoyt, J. J., Asta, M. & Karma, A., *Physical Review Letters*, **86**, 5530 (2001)

80. Müller, P. & Métois, J.J., *Thin Solid Films*, **517** 65 (2008)

81. Collins, J. B. & Levine, H., *Physical Review B*, **31**, 6119 (1985)

82. Langer, J. S., in : Grinstein, G., Mazenko, G.,(Eds.), *Directions inc Condensed Matter*, World Scientific, Singapore, 164 (1986)

83. Karma, A., *Phase Field Methods*, in: Buschow, K. J. H., Cahn, R. W., Flemings, M. C., IIschner, B., Cramer, E. J. & Mahajan, S. (Eds) *Encyclopedia of Materials: Science and Technology*, **7**, Elsevier, Oxford, 6873 (2001)

84. Bottinger, W. J., Warren, J. A. L., Beckermann, C. & Karma, A., *Annual Review of Materials Research*, **32**, 163 (2002)

85. Asta, M., Hoyt, J. J. & Karma, A., *Physical Review B*, **66**, 100101 (2002)

86. Morris, J. R., *Physical Review B*, **66**, 144104 (2002)

87. Sun, D. Y., Asta, M. & Hoyt, J.J., *Physical Review B*, **69**, 174103 (2004)

88. Sun, D. Y., Mendelev, M. I., Becker, C. A, Kudin, K., Haxhimali, T., Asta, M., Hoyt, J.J., Karma, A. & Srolovitz, D. J., *Physical Review B*, **73**, 024116 (2006)

89. Ravelo R & Baskes M *Physical Review Letters* **79** 2482 (1997)

90. Berroukche A , Soudini B & Amara K *Int. J. Nanoelectronics and Materials* **1** 41 (2008)

91. Tersoff J., *Physical Review Letter,* **56** 632 (1986)

92. Baskes M I *Physical Review B (Condensed Matter)* **46** 2727 (1992)

93. Plimpton S J, *Lammps web page, 2003*
http://www.cs.sandia.gov/ sjplimp/lammps.html.

94. Askeland, D. R. & Phulé, P. P., *The science and engineering of materials*, Nelson, USA (2006)

95. Gale, G.F. & Totemeier, T.C., *Smithells Metals Reference Book*, Elsevier, Oxford (2004)

96. Morris, J.R., Wang, C.Z., Ho, K.M. & Chan, C.T., *Physical Review B,* **49**,3109 (1994)

97. Mishin Y *Acta Materialia* **52** 1451 (2004)

98. Williams P L, Mishin Y & Hamilton J C *Modeling and Simulation in Materials Science and Engineering* **14** 817 (2006)

99. Hoyt J J, Garvin W J, Webb III E B & Asta M *Modeling and Simulation in Materials Science and Engineering* **11** 287 (2003)

100. Ramalingam H, Asta M, Van de Walle A & Hoyt J J Interface Science **10** 149 (2002)

101. Hafner J *Physical Review B (Solid State)* **10** 4151(1974)

102. Ihm J & Cohen M L *Physical Review B (Condensed Matter)* **23** 1576 (1981)

103. Cheong BH & Chang K J *Physical Review B (Condensed Matter)* **44** 4103 (1991)

104. Corkill J L, Garcia A & Cohen M L *Physical Review B (Condensed Matter)*, **43** 9251 (1991)

105. Christensen N E & Methfessel M *Physical Review B (Condensed Matter)* **48** 5797 (1993)

106. Chun Yu, Junyan Liu, Hao Lu & Junmei Chen *Solid State Communications* **140** 538 (2006)

107. Kittel C *Introduction to Solid State Physics* New York Wiley 6th ed (1986)

108. Barrett C S & Massalski T B *Structure of Metals* McGraw-Hill New York (1966)

109. *Thermochemical Properties of Inorganic Substances*, Springer-Verlag, Berlin (1973)

110. Tack J L & Ford D M *Journal of Molecular Graphics and Modeling* **26** 1269 (2008)

111. Clancy T C, Frankland SJV, Hinkley JA & Gates TS *Polymer* **50** 2736 (2009)

112. Turnbull, D., *Journal of Chemical Physics*, **18,** 768 (1950)

113. Gündüz, M. & Hunt, J. D., *Acta Metallurgica,* **33**, 1651 (1985)

114. Böyük, U., Engin, S. & Maraslı, N., *Journal of Alloys and Compounds*, **476** 213 (2009)

115. Bayender, B. et al., *Materials Science and Engineering,* **270**, 343 (1999)

116. Bayender, B. et al., *Journal of Crystal Growth,* **194** 119 (1998)

117. Marasli, N., Keslioglu, K., & Arslan, B., *Journal of Crystal Growth,* **247**, 613 (2003)

118. Napolitano, R.E., Liu, S. & R. Trivedi, *Interface Science* **10** 217 (2002)

119. Napolitano, R.E. & Liu, S., *Phys. Rev. B,* 70 (2004)

120. G. Wulff, Z. Krist. **34**, 449 (1901).

121. Esin, V. O., Pankin, G. N. & Nasyrov, R. S., *Sov Phys Crystallogr.*, **18,** 246 (1973)

122. Nash, G.E.& Glicksman, M.E., *Acta Metallurgica*, **22**, 1283 (1974)

123. Trivedi, R.& Tiller, W. A., *Acta Metallurgica*, **26**, 671 (1978)

124. Pokhorova, M. F., *Inzhenerno – fizicheskii Zhurnal*, **61**, 808 (1992)

125. Broughton, J.Q. & Gilmer, G.H., *Journal of Chemical Physics* **84,** 5759 (1986).

126. Davidchack, R.L. & Laird, B.B., *Physical Review Letter* **85** 4751 (2000).

127. Hoyt, JJ, Asta, M & Karma, A., *Physical Review Letter* **86**, 5530 (2001)

128. Davidchack, R.L.& Laired, B.B., *Physical Review Letter*, **85**, 4751 (2000)

129. Mu, Y., Houk, A. & Song, X. Y., *Journal of Chemical Physics*, **109**, 6500 (2005)

130. Morris, J.R., *Physical Review B* **66** 144104 (2002) .

131. Foiles, S. M. & Hoyt, J. J., *Acta Materialia* **54**, 5531 (2006)

132. Morris, J.R., Song, X.Y., *Journal of Chemical Physics,* **119**, 3920 (2003)

133. G. Wulff, Z. Krist, 34, 449 (1901)

134. Willnecker, R., Herlach, D.M. & Feuerbacher, B., *Physical Review Letters*, **62**, 2707 (1989)

135. Lum, J. W., Matson, D. M. & Flemings, M. C., *Metall. Mater. Trans. B.*, **27B**, 865 (1996)

136. Bragard, J., Karma, A., Lee, Y. H. & Plapp, M., *Interface Science*, **10**, 121 (2002)

137. Glicksman, M.E. & Schaefer, R.J., *Journal Crystal Growth* **1** 297 (1967).

138. Rodway, G.H. & Hunt, J.D., *Journal of Crystal Growth* **112** 554 (1991)

139. Broughton, J.Q., Gilmer, G.H. & Jackson, K.A., *Physical Review Letter* **49** 1496 (1982)

140. Wilson, H. A., *Philosophical Magazine*, **50**, 238 (1900)

141. Frenkel, J., *Phys. Z. Sowjetunion* **1** 498 (1932)

142. Turnbull, D.& Bagley, B. G., *Solid State Chemistry*,**5**, 526 (1975)

143. Coriell, S. R.& Turnbull, D., *Acta Metallurgica,* **30**, 2135 (1982)

144. Burke, E., Broughton, J.Q. & Gilmer, G.H., *Journal of Chemical Physics* **89** 1030 (1988)

145. Bragard, J., Karma, A., Lee, Y.H. & Plapp, M., *Interface Science* **10** 121 (2002)

146. Dvinyaninov, M M & Romanenko, V. N., *Fizika*, **4** 10 (1991)

147. Kramer, J J & Tiller, W A, *The Journal of Chemical Physics*, **42** 257 (1965)

148. Briels, W.J., Tepper, H.L, *Physical Review Letters*, **79** 5074 (1997)

149. Huitema, H.E.A., Vlot, M.J. & Van Der Eerden, J.P. *Journal of Chemical Physics*, **111** 4714 (1999)

150. Hoyt, J.J., Sadigh, B., Asta, M., Foiles, S.M. *Acta Materialia*, **47** 3181 (1999)

151. Tepper, H.L., Briels, W.J. *Journal of Chemical Physics*, **115** 9434 (2001)

152. Yesin, V. O., Pankin, G. N. & Tarabayev, L. P., *Fiz. Metal. Metalloved*, **36**, 1256 (1974)

153. http://www.dur.ac.uk/sharon.cooper/lectures/cryskinetics/handoutsalla.html